Nuclear Materials and Energy 29 (2021) 101085

Contents lists available at ScienceDirect

Nuclear Materials and Energy

journal homepage: www.elsevier.com/locate/nme

Radiation damage evolution in pure W and W-Cr-Hf alloy caused by 5 MeV Au ions in a broad range of dpa

A. Macková [a,b,*], S. Fernandes [a,k], J. Matejíček [c], M. Vilémová [c], V. Holý [d,e], M.O. Liedke [f], J. Martan [g], M. Vronka [h], M. Potoček [i,j], P. Bábor [i,j], M. Butterling [f], A.G. Attallah [f], E. Hirschmann [f], A. Wagner [f], V. Havránek [a]

[a] Nuclear Physics Institute of the Czech Academy of Sciences, 250 68 Husinec - Řež, Czech Republic
[b] Department of Physics, Faculty of Science, J.E. Purkyne University, Pasteurova 3632/15, 400 96 Ústí nad Labem, Czech Republic
[c] Institute of Plasma Physics of the Czech Academy of Sciences, Za Slovankou 3, 18200 Prague, Czech Republic
[d] Department of Condensed Matter Physics, Faculty of Mathematics and Physics, Charles University Ke, Karlovu 5, 121 16 Prague 2, Czech Republic
[e] Faculty of Science, Masaryk University, Kotlářská 2, 61137 Brno, Czech Republic
[f] Helmholtz-Zentrum Dresden - Rossendorf, Institute of Radiation Physics, Bautzner Landstraße 400, 01328 Dresden, Germany
[g] New Technologies - Research Centre, University of West Bohemia, Univerzitní 8, 301 00 Plzeň, Czech Republic
[h] Institute of Physics of the Czech Academy of Sciences, Na Slovance 1999/2, 18221 Prague, Czech Republic
[i] Central European Institute of Technology, Brno University of Technology, Purkyňova 656/123, 612 00 Brno, Czech Republic
[j] Institute of Physical Engineering, Faculty of Mechanical Engineering, Brno University of Technology, Technická 2896/2, 616 69 Brno, Czech Republic
[k] Sorbonne Université, CNRS, Institut des NanoSciences de Paris, INSP, SAFIR, F-75005 Paris, France

ARTICLE INFO

Keywords:
W and W-Cr alloy ion irradiation
Radiation damage
Fusion materials
Structure analysis of defects

ABSTRACT

Pure W and W-Cr-Hf alloy which are prospective materials for nuclear fusion reactors, such as DEMO, were irradiated at room temperature with 5 MeV Au^{2+} ions with fluences between 4×10^{14} and 1.3×10^{16} ions.cm^{-2} to generate various levels of lattice damage from about units up to tens of dpa. The distinct character of radiation damage accumulation, microstructure and defect nature have been observed in both pure W and W-Cr-Hf alloys, the latter exhibited interesting ability of damage reorganisation and defect size decrease at the higher ion fluences as determined by positron annihilation spectroscopy (PAS). High radiation damage rate in the irradiated layer has been evidenced in the W samples already at the lower Au-ion fluences compared to W-Cr-Hf samples, where the damage increased in steps with the increasing Au-ion fluence. The distinct defect accumulation was accompanied with the different Au-ion implanted distribution in the irradiated layer determined by Secondary Ion Mass Spectrometry (SIMS) as well as the thermal properties have shown the consequent worsening in the depth in good agreement with the Au-depth concentration profiles. TEM corroborated above mentioned findings, where the sub-surface layer exhibited defect release after the irradiation, the maximum of dislocation loop density has been identified in the depth according the predicted dpa (displacement particles per atom) maximum for the lower Au-ion fluences. Moreover, TEM shows the dislocation density band structure appeared in W-Cr-Hf samples exhibiting the high density defect band according the projected range of the Au-ions simultaneously with the additional layer with larger isolated dislocations pronounced in the higher depth as a growing function of Au-ion fluence. Such phenomenon was not observed in W samples.

Introduction

Fusion reactor material technology is seen to be a key for successful realization of fusion reactors [1,2]. Considerable neutron damage at rates of 3–4 dpa (displacement per atom)/year [3] and steady impacting plasma loads pose a threat to the plasma facing materials. Tungsten (W) is a forerunner for the plasma facing components, such as the divertor and the first wall, given its high melting point (3695 K), high thermal conductivity and relatively low sputtering [4,5]. In fact, novel solutions with W, such as W-fiber composites, mixed W-Cr-based alloys and functionally graded layers of W and Cu are being proposed as solutions for handling the thermal and radiation load [6]. Recently, heavy ion

* Corresponding author.
E-mail address: mackova@ujf.cas.cz (A. Macková).

https://doi.org/10.1016/j.nme.2021.101085
Received 13 August 2021; Received in revised form 13 October 2021; Accepted 1 November 2021
Available online 3 November 2021

irradiation damage in fusion reactor materials started to be in focus [7,8], as it can mimic various stages of the radiation damage without material activation. The presence of defects in materials applied in fusion reactors can have a significant effect on their properties, performance and lifetime under operational conditions. Therefore, the characterization of irradiated materials can lead to a better understanding of defect formation and help find ways to minimize or eliminate it.

Tungsten is a refractory metal, widely used in demanding industrial applications, usually in high-temperature environment and this stems out of its high melting point, good thermal conductivity and high strength at elevated temperatures [9]. Nevertheless, tungsten also possesses high ductile–brittle transition temperature, recrystallization temperature significantly lower than the melting point and poor oxidation properties. New materials and production methods such as mechanical alloying are applied to tungsten; they allow tailoring the grain size, formation of dense dislocation structures and formation of full solid solution with elements that possess otherwise limited solubility in tungsten lattice. Frequently this method is used to improve mechanical properties or to introduce new properties, such as self-passivation in oxidizing environment [10,11]. Irradiation effects on tungsten materials were reviewed in [5]. In general, radiation damage leads to degradation of both mechanical and thermal transport properties. In [12], fracture toughness of two tungsten materials conforming to ITER specifications, processed by powder metallurgy and plastic deformation, was found to progressively decrease with irradiation dose up to 0.7 dpa. Likewise, neutron irradiation to 0.24 and 0.7 dpa led to fracture toughness decrease in spark plasma sintered tungsten, causing a shift of about 300 °C in the ductile-to-brittle transition temperature [13]. Compared to neutron irradiation, ion irradiation brings several advantages, mainly the ability to achieve significant dpa faster and the lack of activation that complicates post-irradiation handling and investigation of neutron-irradiated materials [14]. The general approach of using significantly higher ion energies for implantation and radiation damage studies in plasma facing materials is accepted in most cases in order to circumvent the complications associated with low ion energy implantation (e.g. for electron microscopy, nano-indentation, and thermal transport measurements [15–17]).

W samples irradiated with 1–4 MeV Re and exposed in He plasma were investigated in Ref. [18] and it was found that the hardness increases for all samples relative to the unmodified reference. The results indicate that after sub-sequent He ion irradiation, the He was trapped in vacancies and formed He nano-bubbles in the W matrix, resulting in increased material hardness. Armstrong et al. [19] investigated changes to the mechanical properties in pure W samples resulting from sequential self- ion implantation up to 13 dpa followed by He-ion implantation. It was suggested that the self-ion implanted region contained pre-existing dislocation loops and that He trapped in distributed vacancies gives stronger hardening than He trapped in vacancies condensed into dislocation loops. Recently Zhang et al. [20] used nano-indentation to investigate the hardening effect of as-received and recrystallised W samples using 6.4 MeV Fe^{3+} and it was found that Fe^{3+} ion irradiation resulted in hardening in all W samples.

Ions lose their energy via ionization (electronic stopping) and collisions with nuclei of irradiated targets (nuclear stopping). In swift heavy ions (SHI) irradiation, typically featuring enormous electronic energy transfer via ionization [21], e.g. by irradiation with a 60 keV.nm^{-1} SHI, the formation of elongated interstitial dislocation loops with a halo of isolated vacancies was predicted by molecular dynamics [19]. However, lower ion energies of several MeV are advantageous as the penetrating ions modify the near subsurface layer of <1 μm and such modified layers are easier to be investigated with the above mentioned surface analytical methods as well as to the requested dpa due to the significantly higher nuclear stopping at the lower ion energies.

Extensive research is focused nowadays on the synthesis of materials with an ultra-fine-grained microstructure, and on the synthesis of W-based alloys with other element. The researchers aim at improving the radiation resistance, mechanical properties and oxidation resistance of tungsten-based materials in the case of a reactor accident. Main strategies for achieving such an improvement is the production of ultra-fine-grained structure, control of impurity and grain size during sintering, and addition of oxide forming elements. Thus, oxidation behaviour and mechanical properties can be improved by addition of Cr and Hf, respectively. Hf controls the grain growth during sintering and prevents oxidation of Cr by formation of HfO_2 particles at grain boundaries and lowering the oxygen content in the W-Cr alloy [22,24].

The authors in Ref. 23 studied ion irradiation on fine- and coarse-grained tungsten, focusing on the effects of dpa rate and temperature on the irradiation damage. It has been shown that grain size, number of grain boundaries and their orientation caused different defect sink efficiencies and that the grain boundaries can improve radiation tolerance due to the defect annihilation [23]. The radiation damage induced by 3 MeV Cu^{+} at RT and 1050 K on thin foils of pure W of nano- and micrometer grain sized was studied from 0.25 to 4 dpa for two-level dpa rates [23]. The total radiation damage was quantified from the density and average area of two loop types ⟨1 1 1⟩ and ⟨1 0 0⟩ present in W in the same high magnified area of bright-field TEM images. Both W grades underwent a 1-D interstitial loop migration during Cu-ion irradiation at RT, a dislocation loop rafting phenomena and the formation of a uniform distribution of voids across the different grains with a dominant presence of ⟨1 0 0⟩ loops which are suggested to be of vacancy type. The nanocrystalline W reached higher loop densities (~3×) after irradiation to 1 dpa at RT and at 1050 K and lower average loop areas than the microcrystalline W, simultaneously the loop density increased up to 2–3 dpa, but at 4 dpa it decreased significantly due to loop coalescence associated to growth of vacancy loops on the void sites, whereas in the microcrystalline W the loop coalescence occurred at 0.25 dpa.

Our intention was to collect the broad range of dpa values ranging from 1 up to 100 dpa which is rather scarce in literature for W and W-Cr-Hf samples. The Au-ions with high mass cause the denser collision cascade, thus the desired dpa values are reachable using the lower ion fluence compared to lighter ions.

For instance, when we compare calculation for Cu-ions with energy 5 MeV and Au-ions 5 MeV we can get in maximum 4–5 displaced atoms/10^{-10}m.ion in the depth about 1,5 μm and 20–25 displacements/10^{-10}m.ion in the depth about 0,5 μm, respectively. High fluence implantation means the longer time of exposure which can be instrumentally demanding, it can cause additional complex phenomena of defect migration, common interaction and temperature rise in the sample etc. The heavy ions are stopped in the shallower depth below the surface, the more localised defects and implant distribution is achieved. Increasing ion energy implies the broader depth distribution of ions and defects. The shallower modified layers can be more advantageous for some of analytical methods such as PAS, where we want to follow the whole damage profile.

Based on above mentioned we decided to investigate and compare W and W-Cr-Hf alloys under the irradiation conditions using Au-5 MeV ions in order to: i) follow radiation damage accumulation for the wide range of dpa from 0.8 to 98 being rare in literature; ii) understand the nature of defects created under such irradiation conditions, structure modification and internal morphology (microstructure) in the buried layer and beyond for both materials using X-ray diffraction (XRD), Positron Annihilation Spectroscopy (PAS) and Transmission Electron Microscopy (TEM); iii) follow and discuss thermal transport properties as direct consequence of structural modification after irradiation.

Experimental

The pure W samples were cut by electro-discharge machining from a 38 × 38 mm ingot produced by Plansee by powder metallurgy and forging (ITER-qualified grade, 99.97% purity, C < 30 ppm, O < 20 ppm), followed by stress relieving. It was polished by electro-polishing previously to the irradiation. W produced by Plansee according to ITER

specifications is a widely used 'reference' material, while the W-Cr-Hf alloy is a developmental material, produced in a laboratory, whose aim is to improve specific properties over pure W. The next studied material, W-Cr-Hf, was prepared by mechanical alloying and spark plasma sintering. Alloyed powder was prepared in a planetary ball mill Pulverisette 5 (Fritsch, D) from the following powders: W (1.2 μm average powder size, purity > 99.5%), Cr (0.4 μm average powder size, purity > 99%) and Hf (bimodal 15 and 45 μm, purity > 99.2%). The powders were processed in tungsten carbide vials with tungsten carbide grinding balls with ball to powder ratio 11: 1. Argon was used as a protective atmosphere preventing oxidation during the milling process. The overall milling time for a W-10Cr-1Hf (wt %) alloy was 28 h at a speed of 240 rpm. A spark plasma sintering machine SPS 10-4 (Thermal Technology, USA) was used to consolidate the mechanically processed powder at 1750 °C and 70 MPa with 3 min. hold time at the sintering temperature; tungsten foil surrounding the sintered powder was used as a carbon contamination barrier [24]. As a suitable electro-polishing procedure was not found for the W-Cr-Hf alloy, it was polished only mechanically. It was concluded in our previous findings that the matrix of the W-Cr-Hf alloy consists of only one W-rich phase. HfO_2 particles in monoclinic form were evidenced in W-Cr-Hf alloys in [24].

Ion irradiation and SRIM calculation

Irradiation of the pure W and W-Cr-Hf samples was performed with 5 MeV Au ions from Tandetron accelerator at ion implantation instrument enabling homogeneous distribution of ion fluence over the sample area. The samples were mounted using Cu-tapes to improve heat dissipation, however the collection of the ion fluences was realized in couple of minutes and hours for the lowest and highest fluences, respectively. We didn't observe any significant increase of the sample temperature during the implantation. The 5 MeV Au-ions are heavy enough to introduce collision cascade and displacement in the layer useful for many surface analytical methods, simultaneously nuclear stopping is large enough to create a significant number of displaced W atoms. The calculation of electronic and nuclear stopping caused by 5 MeV Au ions was realized with the SRIM software [25] and it is presented in Fig. 1a, b for W and W-Cr-Hf materials, respectively, taking into account the elemental composition and matrix parameters from f.

Various Au-ion fluences were used to reach broad range of radiation damage to study the defect structure over a heavy ion damaged region. The irradiation conditions, SRIM calculation parameters (the ion implantation fluence, the elemental displacement energies E_D, the projected range R_P ions with the standard deviation ΔR_P) and the material properties such as bulk density and atomic composition are summarized in Table 1. The appropriate W, Cr vacancy depth profiles and the Au distribution were determined using the Quick Kinchin-Pease (QP) and Full Cascade (FC) models [25], under the assumptions of a constant threshold displacement energy for each of the elements as given in Table 1, based on existing W experimental data [26] and on simulated data for the W-Cr-Hf alloy [27,28].

Table 1
Summary of the ion implantation experiment parameters and W and W-Cr-Hf sample properties. SRIM calculated projected ranges R_P, dpa (displacement for atom – the range of values), E_d displacement energies.

Material	Pure W (min. 99.97 %)		W-Cr-Hf	
Density (g.cm^{-3})	19.30		16.7	
E_d (eV)	W: 90 ± 18		W: 90 ± 18 Cr: 40 ± 8 Hf: 61 ± 12	
Composition (% mass / % atomic)	100		W: 89 / 70.981 Cr: 10 / 28.198 Hf: 1 / 0.821	
Projected range of Au ions	R_P = 321		R_P = 349	
Deviation of projected range (nm)	ΔR_P = 118		ΔR_P = 119	
Fluence (ions.cm^{-2}) / corresponding dpa range	4×10^{14}	0.8–3	4×10^{14}	1–4
	1.3×10^{15}	3–10	1.3×10^{15}	3–11
	5×10^{15}	10–38	5×10^{15}	14–42
	1.3×10^{16}	26–98	1.3×10^{16}	32–101

It can be concluded that nuclear energy stopping is employed comparably to electronic stopping being in order of several keV.nm^{-1} and comparable for both used materials. The total number of vacancies is comparable for both materials and the maximum of the vacancy depth profile is closer to the surface in comparison with the depth of Au ion projected range. The modified layer thickness is estimated to be about 600 nm, however this calculation does not take into account any defect migration specific in a given microstructure as well as gradual radiation damage in a dynamic manner. SRIM calculation for W-Cr-Hf samples was provided using the volume density given in Table 1 which can suffer higher uncertainty, thus it could cause the higher discrepancy comparing the predicted and the experimental Au-concentration maximum depth.

Defect accumulation analysis using PAS

Positron annihilation spectroscopy (PAS) is a powerful technique providing unique information about open-volume lattice defects [29,30]. In the present work PAS investigations were carried out either using *fast* positrons emitted by a ^{22}Na radioisotope or using *slow* positrons obtained by moderation of fast positrons. Doppler broadening variable energy positron annihilation spectroscopy (DB-VEPAS) measurements were carried out using a ^{22}Na-based monoenergetic positron beam, which serves for offline experiments. DB-VEPAS measurements have been conducted at the apparatus for in-situ defect analysis (AIDA)

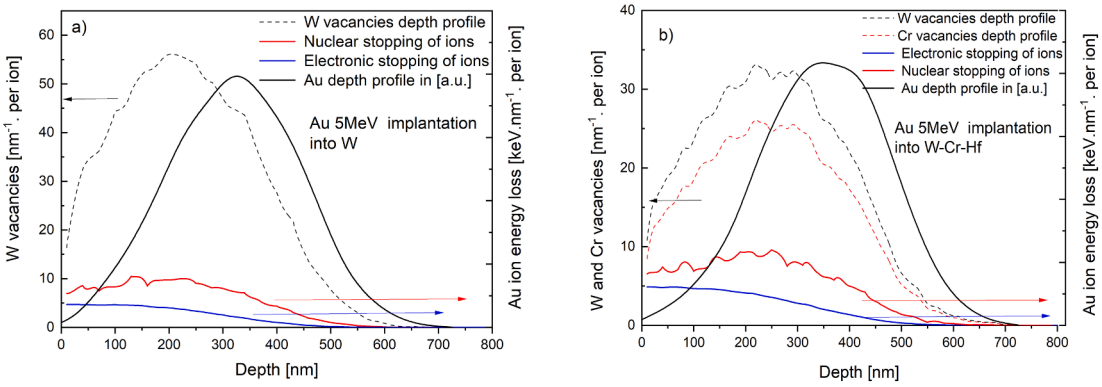

Fig. 1. SRIM calculated Au-concentration depth profiles, nuclear and electronic stopping of 5 MeV Au ions as well as W, Cr vacancy depth profiles per nm and ion are presented for W in a) and for W-Cr-Hf alloy in b).

[31] of the slow positron beamline (SPONSOR) [32]. Positrons have been implanted into a sample with discrete kinetic energies E_p in the range between 0.05 and 35 keV, hence realizing a depth profile starting at the surface down to about 1 μm in case of tungsten. Measurements of the specimens were carried out at room temperature under vacuum pressures $\leq 2 \times 10^{-7}$ mbar. By DB-VEPAS it was possible to access the relative changes of defect concentration induced by Au-ion irradiation across the implantation profile and beneath. Variable energy positron annihilation lifetime spectroscopy (VEPALS) measurements were conducted at the Mono-energetic Positron Source (MePS) beamline at HZDR, Germany [33,34]. The spectra were deconvoluted using the non-linearly least-squared based package PALS fit fitting software [35] into two or three discrete lifetime components, which directly evidence two or three different defect types (sizes). The corresponding relative intensities reflect to a large extent the concentration of each defect type (size). In general, positron lifetime decreases with the defects size: the larger is the open volume, the lower is the annihilation probability and the longer it takes for positrons to be annihilated with electrons [36]. The positron lifetime and its intensity has been probed as a function of positron implantation energy E_p or, in other words, the implantation depth (thickness).

Structure analysis by XRD

In order to study the structure modification of the pristine and irradiated samples, X-ray diffraction (XRD) was used. The measurements have been carried out on a PaNalytical 1.5 kW sealed-tube generator using CuKα_1 characteristic radiation, equipped with a primary parabolic multi-layered mirror combined with a 2xGe220 channel-cut monochromator. A 0.04 rad Soller slit and a one-dimensional detector in the scanning mode were used on the secondary side. Using this non-focusing high-resolution setup we measured detailed symmetric 2Θ/α-scans around several diffraction maxima, as well as long-range scans comprising a large 2Θrange (not used here). For the CuKα_1 radiation, the penetration depth of the incoming X-ray beam in tungsten increases from L ≈ 1 μm for the incidence angle $\omega = 2\Theta/2 = 10$ deg up to L ≈ 8 μm for $\omega = 90$ deg. In the symmetric scattering geometry, the information depth from which the diffracted signal is collected equals L/2.

Au concentration depth profiles analysed by TOF-SIMS

Secondary Ion Mass Spectrometry (SIMS) is very powerful tool for depth profiling of all elements with very low detection limits with superior depth resolution of about 1 nm and detection limits 10^7 –10^{10} at. cm^{-2} down to 1 ppm bulk concentration in depth profiles. The crucial point is the sputtering procedure, then the elemental depth profiling can be realized over larger depths than those offered by other surface depth profiling analytical techniques. The SIMS measurements were performed by using a Time of Flight (TOF)-SIMS - IONTOF instrument in the depth profiling mode using negatively charged secondary ions. A source of Bi^+ ions were used with the following parameters: impact energy of 30 keV, impact angle of 45°, pulsed primary current of ~ 3 pA, raster size 50 μm × 50 μm. The Cs^+ co-sputtering was performed at the interlaced regime with a crater size of 150 μm × 150 μm and an impact angle of 45°. The parameters of the secondary ion optics were the following: an extraction voltage of 3 kV, a cycle time of 60 μs, and a mass resolving power of ~ 7000 at Au peak. The base pressure in the analytical chamber was ~ 5×10^{-10} mbar. During the measurements, the analytical chamber was at ~ 5×10^{-9} mbar [37]. The TOF-SIMS was used due to its high sensitivity and precision in measuring the Au depth distribution in the tested samples after Au-ion irradiation for comparing with the theoretical calculation performed by SRIM, see chapter 2.1.

Internal structure analysis by TEM

The internal structural morphology of the tested samples after the Au-ion irradiation was investigated by transmission electron microscopy (TEM) and scanning transmission electron microscopy (STEM) to characterize the nanoscale microstructural evolution in the sub-surface layers and relate to the Au depth distribution measured experimentally as calculated by SRIM. Samples for TEM and STEM studies were prepared as lamellas by focused ion beam-SEM technique using an FEI Quanta 3D electron microscope. TEM and STEM observations were carried out by a F|EI Tecnai F20 field emission gun transmission electron microscope operated at 200 kV.

Thermal effusivity

Thermal effusivity as a function of depth was measured by a measurement system based on pulsed photothermal radiometry decribed in details in [38,39]. It uses a pulsed laser to heat the material surface and fast infrared detector to observe temperature decrease after the laser pulse. From the temperature decrease with time in the nanosecond time range, the thermal effusivity in depth of hundreds of nanometres was evaluated.

Results

PAS and XRD analyses

PAS and XRD analyses of the Au-ion implanted W

In PAS analysis of defect distribution across samples thickness the VEPFit code [40] has been utilized to determine the so-called positron diffusion length (L_+), a parameter inversely proportional to defect concentration. Increase in the defect concentration leads to a shortening of the positron diffusion length. DB-VEPAS measurements of the pure tungsten sample show the existence of large initial defect concentration connected to the very short positron diffusion length ($L_+ < 1$ nm) in the subsurface region about 74 nm thick and much better crystal quality deeper than 74 nm (L_+~85 nm). Additionally, VEPALS analysis enables positron life time τ measurement being directly connected to defect size. Two parameters were fitted as a function of the positron energy E_p, that is a function of the depth: S (positron annihilation with low electron momentum fraction; valence electrons) scales with positrons trapped at open-volume defects and W (positron annihilation with high electron momentum fraction; core electrons) indicates defects atomic surrounding. When positrons are trapped at vacancy defects the probability of their annihilation with valence electrons possessing low momentum values increases, while the probability of annihilation with core electrons with high momentum values decreases. This leads to growing S and decreasing W, which is also affected by chemical environment at the site of positron annihilation. $S(E_p)$ curves and their fits using the VEPfit code in dependence on Au ion fluence are presented in Fig. 2 for W samples (upper part). The value of the S-parameter, and hence the concentration of defects, decreases with the depth in the pristine W. The results show that we can recognize three regions: i) the very near subsurface region of about 5 nm (see Fig. 2a – region I) that represents defect surface states and likely oxides; ii) the region about several tens of nm (Fig. 2 – region II from 5 to 74 nm) contains defects in the pristine sample. L_+ increases hence defect concentration decreases. This layer is influenced by Au-induced vacancy creation (compare to the SRIM calculated vacancy depth profiles in Fig. 1); iii) the defect maximum caused by Au ion irradiation is much deeper about 200–400 nm (in region III), where the defect density increase with the Au-ion fluence is observed. This fact is in correspondence with the calculated projected range of Au-ions being about 320 nm (see Table 1). After the Au-ion irradiation; S parameter is lowered in the sub-surface region I., enhanced in the region II. with the damage edge shifted to the depth with the increased Au-ion fluence. Finally, the S parameter shows sudden enhancement and saturation of defect concentration above 4×10^{14} cm^{-2} in the region III (see Fig. 2a).

Interesting is the fact, that with the increased Au-ion irradiation

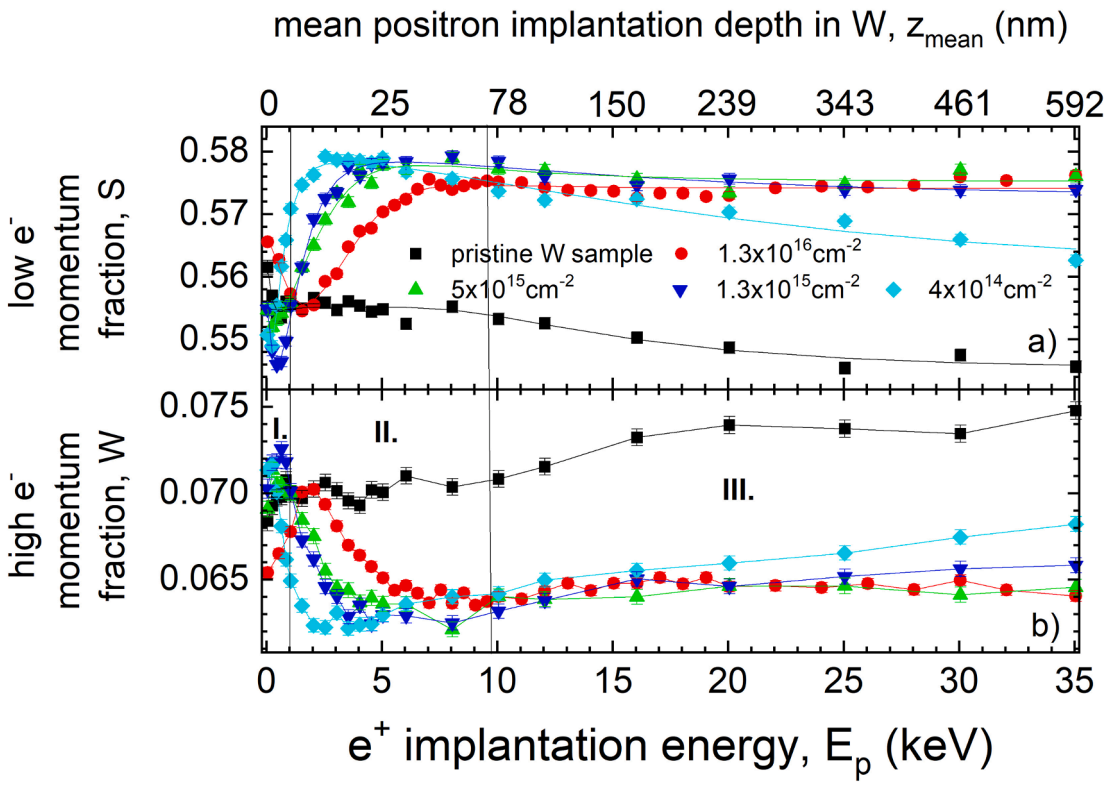

Fig. 2. DB-VEPAS positron lifetime measured S and W parameters as a function of the implanted positron energy E_p and equivalent mean depth for W samples a) and b), respectively.

fluence defect free zone in region II. increases in thickness. The disorder in this layer is released with the increasing Au-ion irradiation fluence or the damage edge is shifted into the depth. Contrary, in the depth of the maximum vacancy creation induced by Au-ions (region III.), the defect density in the pristine sample is lower and in this depth a significant enhancement of disorder (increase of defect concentration and/or size) is observed after the Au-ion irradiation exhibiting sort of saturation effect of the defect concentration with the increased Au-ion fluence. The originally defected layer in sub-surface region II exhibits smaller open volume with the increased Au-ion fluence see Fig. 2. This effect is also documented by the progressively enhanced positron diffusion length L_+ in the sub-surface layer (region II.) which changes with the Au-ion fluence as summarized in Table 2. The sub-surface region II. is positioned in the depth, where vacancy concentration starts to grow caused by Au-ion collisions (recoils) of sample atoms (see Fig. 1). The calculated positron diffusion length L_+ and corresponding defected layer thicknesses are presented in Table 2. After the irradiation with Au-ions L_+ increases with the Au-ion fluence in the subsurface layer which is connected with the release of the existing disorder in the sub-surface layer.

From VEPALS results, two positron lifetime components were observed in all the measured spectra τ_1 (annihilation at dislocations and monovacancies) and τ_2 (annihilation in large vacancy clusters, voids). The positron lifetimes component τ_1 as a function of positron implantation energy E_p in W samples are presented in Fig. 3a, where the sub-surface layer is followed mainly (<100 nm). The value of the shortest lifetime in the pristine W sample, $\tau_1 \approx 160$ ps, is much lower than expected for a mono-vacancy and likely represents dislocations [41]. The second minor (≤10%) lifetime component (not shown), $\tau_2 \sim 340$–410 ps, represents superposition of surface states and larger vacancy clusters likely at grain boundaries [42,43]. After irradiation, τ_1 increases to ~ 200–220 ps (vacancy cluster of 2–3 vacancies [44,45]) and τ_2 to 370–440 ps with an increase of intensity I_1 (see Fig. 3b) and corresponding reduction of intensity I_2 (the relative intensity $I_i = I_1 + I_2$). The weighted average defect size is connected to the average positron life time τ_{av}, where the lifetimes as well intensities play a role via the expression: $\tau_{av} = \sum_i \tau_i . I_i$. The increased positron lifetime components show damage accumulation with the increased Au-ion fluence in the deep implanted layer (region III.). However, very similar intensity of I_1 for the higher Au-ion fluences suggests no variation in defect concentration, but rather a slight change in defect size. We can conclude, that *S* and W parameters in the depth of Au implanted ions (200–400 nm) are comparable for fluences above 1.3×10^{15} cm^{-2}, where we can see differences only in the sub-surface less defected layer thickness (region II.) being thicker with the increased Au-ion fluence. The region below the sub-surface layer (region III.) is likely defect saturated hence variation of defect concentration cannot be detected anymore. However, the increase of defect size due to ions is evident. The drop of average positron lifetime for the largest fluence could be explained as Au accumulation in the material filling the available open volume.

Table 2
Calculated positron diffusion length (L_+) and thickness of the sub-surface layer (region II.) (d) created due to ion irradiation in the pure W samples.

Sample	Irradiation fluence (cm^{-2})	L_+ (nm)	*d* (nm)
W pristine	0	< 1	~74
W irradiated	4.0×10^{14}	< 1	< 2
W irradiated	1.3×10^{15}	~6	~12
W irradiated	5×10^{15}	~10	~29
W irradiated	1.3×10^{16}	~31	~60

The XRD diffraction curves of the pristine and the as-irradiated W samples are presented in Fig. 4, where the peaks related to 110, 200, 211, 220 and 310 reflections are depicted in Fig. 4a, b, c, d, and e, respectively). These diffraction peaks are typical for W in α-phase *bcc* structure [46]. We did not identify significant differences in the shapes and positions of the diffraction maxima for the pristine and irradiated W samples. From the 2Θ positions of the maxima we determined the lattice parameter using the Cohen-Wagner graph method [47], we obtained the values of 3.1656 ± 0.0001 Å, 3.1661 ± 0.0001 Å, 3.1658 ± 0.0001 Å

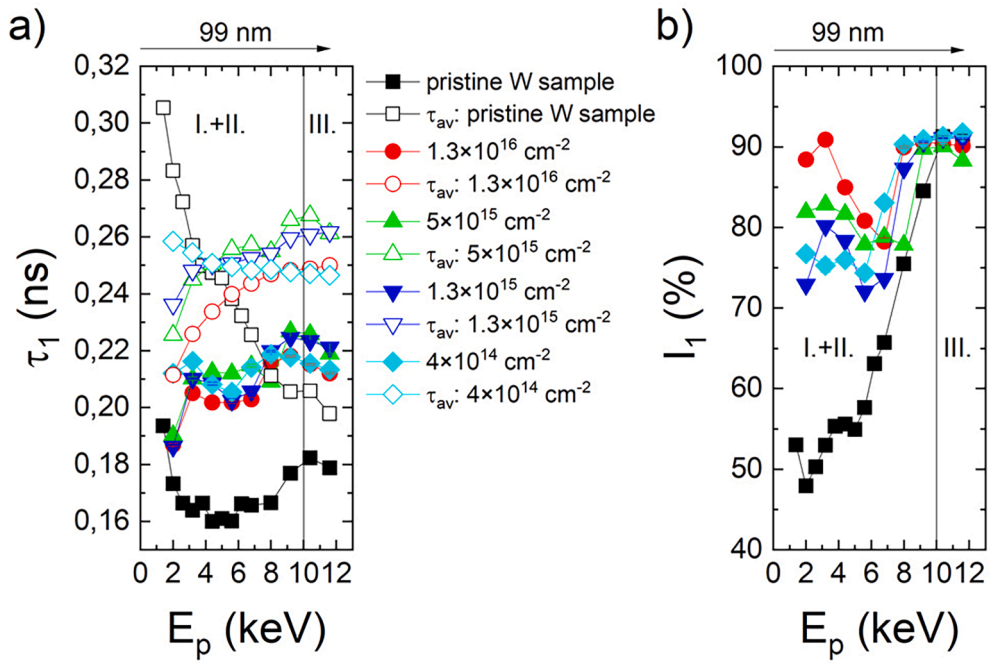

Fig. 3. PALS results: positron lifetime component τ_1 in the Wsamples for the various Au-ion fluences in a) and its relative intensity I_1 as a function of positron energy E_p in b).

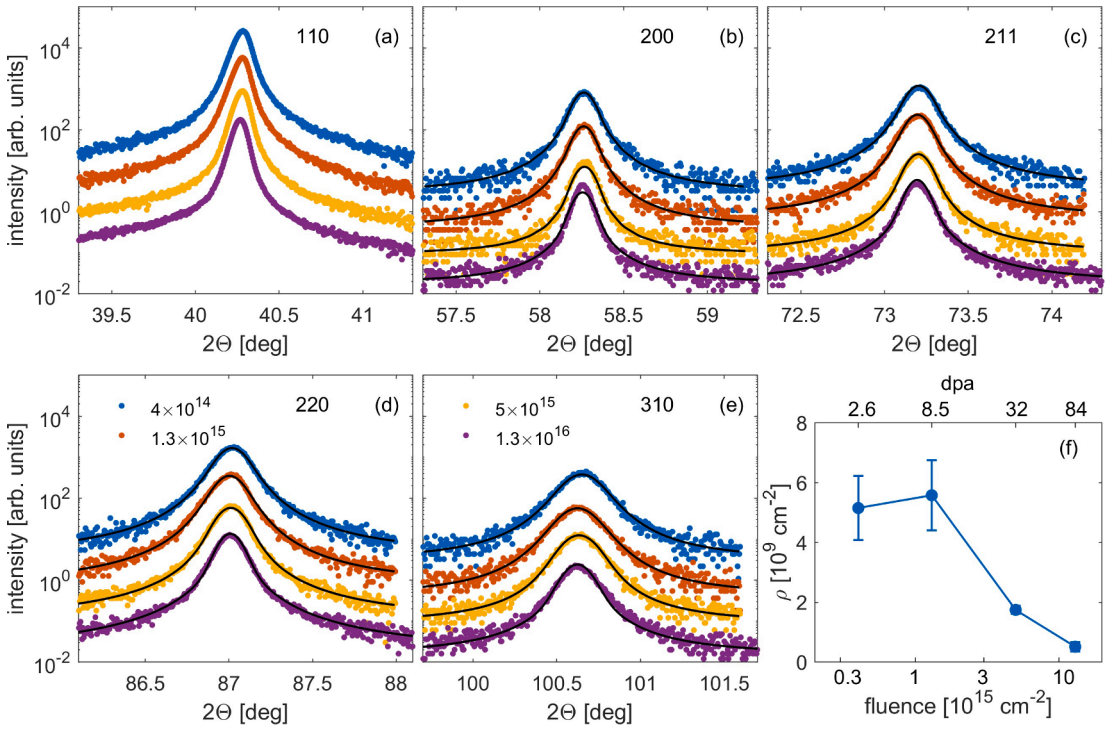

Fig. 4. XRD diffractograms of the W samples irradiated with Au-ions with the various ion fluences with the detail of (110), (200), (211), (220) and (310) diffraction peaks in MR setup in a), b), c), d), e), respectively. The dislocation density determined from XRD analysis using Wilkens model as a function of the Au-implantation fluence in f).

and 3.1658 ± 0.0001 Å for the 4×10^{14}, 1.3×10^{15}, 5×10^{15}cm^{-2} and 1.3×10^{16}cm^{-2} Au-ion fluences, respectively. These values agree quite well to the tabulated value of 3.1652 Å and a possible influence of the Au implantation on the lattice parameter lies below the resolution limit of the method. It has to be emphasized that the information depth of the XRD method comprises several micrometers (see above), so that the measured signal is averaged over the implanted layer and non-implanted substrate. Moreover, due to the symmetric scattering geometry the XRD data are sensitive only to the lattice parameter in the direction perpendicular to the sample surface. We tried to limit the penetration depth by using a strong asymmetric scattering geometry, in which the incidence angle $\omega = 1$ deg was kept constant, and the information depth was roughly 100 nm. We have not detected any measurable shift of the diffraction maxima due to implantation, most likely due

to the fact that the angular resolution was poor in this asymmetric arrangement.

The full widths at half maximum (FWHM) of the diffraction peaks are affected by the vertical size D of crystalline grains (coherently diffracting volumes) and by dislocations. These two effects could be distinguished by comparison of the FWHMs of different reflections; the former effect causes the same broadening of the maxima along the Q_z axis in reciprocal space in different reflections, while the Q_z broadening due to dislocations increases with increasing 2Θ.

The lattice atomic displacement caused by irradiation produces interstitial atom and vacancy, then the dislocations and voids form through the movement and aggregation of interstitial atoms and vacancies. The dislocation can capture many interstitial atoms to form dislocation lines, dislocation walls, dislocation loops and dislocation tangles [46]. The Wilkens dislocation model [48,49] was applied for the estimation of the dislocation density (ρ) of the pure W samples. Using this model we have fitted the shapes of the diffraction maxima 200, 211, 220, and 310, assuming D and ρ as fitting parameters; in Fig. 4a–e the fitted curves are plotted as full black lines. The resulting values of ρ are plotted in Fig. 4f; they decrease slightly for the highest Au-ion fluence, however the whole analysed volume was used for its determination being in order of micrometers, thus the results come from both the irradiated and presumably unaffected layers. The vertical grain sizes were found as follows: 4×10^{14} cm^{-2} (90 ± 2 nm), 1.3×10^{15} cm^{-2} (169 ± 8 nm) and 5×10^{15}cm^{-2} (136 ± 5 nm), 1.3×10^{16}cm^{-2} (142 ± 4 nm).

PAS and XRD analyses of the W-Cr-Hf samples

The parameters *S* and *W* extracted from DB-VEPAS measurements and VEPfit analysis as functions of positron energy (depth) are presented for W-Cr-Hf pristine and the irradiated samples in Fig. 5a and b, respectively. We can identify the very thin subsurface layer – region I (see Fig. 5). W-Cr-Hf pristine sample shows gradual defected layer (see Fig. 5a). It can be concluded, contrary to the Wsamples, that the W-Cr-Hf pristine sample has overall larger concentration of defects in bulk (the positron diffusion length $L_+ \approx 51$ nm, compared to $L_+ \approx 85$ nm for bulk W-film) due to the shorter monotonic $S(E_p)$ decay and contains mostly dislocations and vacancy clusters (as it is shown later by PALS). This effect we observed in the regions II and III as well with the non-negligible depth profile showing defect decrease with the depth (see Fig. 5). The W-Cr-Hf samples exhibited the same effect of the disorder release and the broadening of the defect-free sub-surface layer after the Au-ion irradiation as a function of the ion fluence in region II, similarly to the W samples. However, contrary to the W samples, $S(E_p)$ parameters exhibited gradual decrease in region III., containing Au, with the increasing Au-ion fluence (see Fig. 5), which suggests reduction of the open volume. It is difficult to fit these results in the similar fashion to the W-sample due to limited number of data point in the region II as well as a visible depth profile in region II. More layers would need to be utilized, which usually makes fitting less accurate. Nevertheless, general reduction of the open volume and broadening of the region II, is evident even without $S(E_p)$ fitting.

From PALS results, two positron lifetime components were observed in the measured spectra of the pristine W-Cr-Hf: $\tau_1 \sim$ 150–180 ps (annihilation at dislocations and monovacancies, respectively) and $\tau_2 \sim$ 250–410 ps (annihilation in large vacancy clusters: voids consisting of 5–20 vacancies, respectively). After irradiation with the lowest fluences, the increase of τ_1 suggests a dominant positron annihilation at the size close to monovacancies (4.0×10^{14} cm^{-2}) and dislocations (1.3×10^{15} cm^{-2}) (see Fig. 6a), considering the literature positron lifetime values for pure W [42]. For the 1.3×10^{15} cm^{-2} fluence, the largest concentration of large vacancy clusters has been found, since I_1 decreases (see Fig. 6b). For the two highest fluences used in this study (5×10^{15} and 1.3×10^{15} cm^{-2}), the parameter τ_1 decreases further to 160–180 ps, which was found associated with dislocations, possibly monovacancies. The averaged positron lifetimes τ_{av} are generally lower after the Au-ion irradiation in W-Cr-Hf compared to the W samples (compare Fig. 3b and 6b, respectively), thus the irradiation led to a smaller defect size for W-Cr-Hf, under the same irradiation conditions since their crystalline lattice is similar.

According to the literature, the positron lifetime in W monovacancies is about 200 ps [42] and the positron lifetime in dislocation loop was found to be down to 150 ps [43,50]. We can conclude that at the Au-ion fluence above 5×10^{15}cm^{-2}, the size and defect concentration decrease is connected to the fact, that preferably smaller defects (monovacancies) are created in W-Cr-Hf in comparison to W samples in the irradiated layer. It has to be emphasized, that this phenomenon is observed in the layer investigated with PAS up to 600 nm.

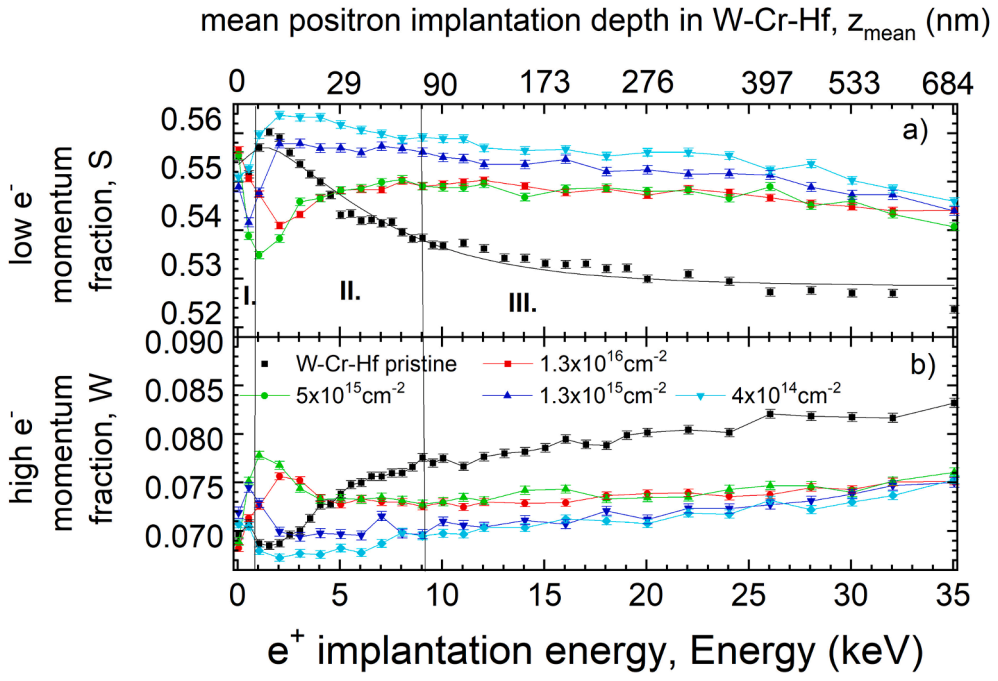

Fig. 5. DB-VEPAS positron lifetime measured S and W parameters as a function of the implanted positron energy E_p and equivalent mean depth for W-Cr-Hf samples.

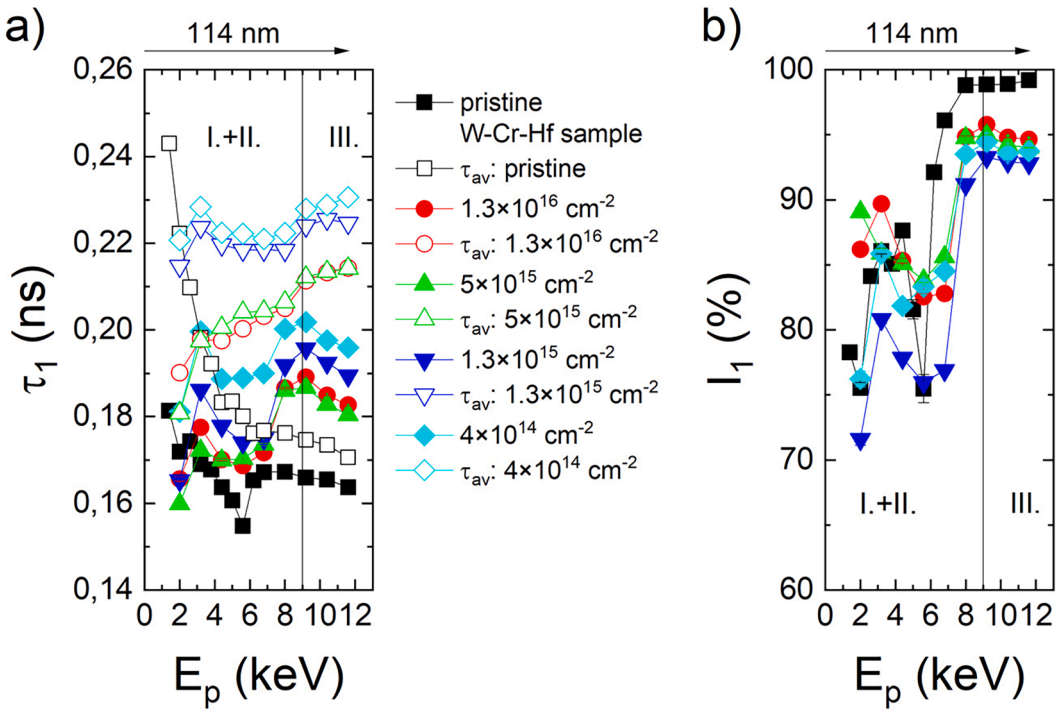

Fig. 6. PALS results: positron lifetime component τ_1 in the W-Cr-Hf samples for the various Au-ion fluences in a) and its relative intensity I_1 as a function of positron energy E_p in b).

XRD diffractograms of the pristine and the irradiated samples W-Cr-Hf are presented in Fig. 7, with the details of diffraction peaks: 110, 211, 220 and 310 in Fig. 7a, b, c and d, respectively. XRD diffractograms of the W-Cr-Hf alloys showed the diffraction peaks typical for α *(W, Cr)* phase as a prevalent in the alloy. It is W-rich phase with Cr in solution [11]. The compositions of *bcc* phases *α(W, Cr)* and *α(Cr, W)* was found e. g. in [11] to be in a proportion of Cr dissolved in W being about 5 wt% (16 at.%), whereas the amount of W in solid solution in Cr being about 41 wt% (17 at.%) being more less in accordance with W-Cr phase diagram in [24]. However, these two phases should be identified with XRD, where typical shift of the diffraction peaks associated with described phases would have to be identified [11]. In our case we didn't observe the latter one phase (Cr-rich phase) in our samples which was consistent with our previous study focused on the W-Cr-Hf alloy preparation [24]. However, it was concluded in our previous findings that the matrix of the W-Cr-Hf alloy consists of only one W-rich phase; the second phase is connected to particles as HfO_2 in monoclinic form at matrix grain boundaries. Therefore, W-Cr solution formed by mechanical alloying was preserved during spark plasma sintering and no chromium was expelled to form Cr-rich phase. Hf role lays mainly in a grain size control to avoid large grain growth. Such single-phase composition of W-Cr alloy is unique, as processing by conventional sintering methods such as HIP (Hot Isostatic Pressing) leads to the development of a Cr-rich phase [11,24].

Newly in this experiment, we can identify two phases with the very near lattice parameters in XRD analysis of W-Cr-Hf (see Fig. 7). The two-peak structure appearance cannot be connected to the presence of the stable spinodal decomposition, when in a thermodynamically unstable initial state long-wavelength delocalized small-amplitude statistical fluctuations grow spontaneously in amplitude as the time after the quench increases. The twin phases produced by the spinodal decomposition of a supersaturated solid solution differ in composition from the parent phase, but have basically the same crystal structure, but this effect was excluded in [11,24]. However, this effect of the two-component diffraction peaks in XRD diffractograms seems to be real not an artifact. It implies the lattice parameters misfit connected to very close but distinct W concentration in *bcc* α*(W, Cr)* phases estimated as 77 and 82 at.% according the W-Cr phase diagram presented in [11] (see Fig. 7 – the vertical lines show the various W-concentration in atomic %). Vertical grain sizes of the crystalline phase with smaller lattice component decreases from about 20 ± 2 nm in the pristine sample to about 5 ± 0 nm in the sample irradiated at the Au-ion fluence 5×10^{15} cm^{-2}. Simultaneously, the vertical grain sizes of the phase with the higher lattice constant increases with the irradiation fluence from 31 ± 2 nm to 82 ± 11 nm for pristine and irradiated sample, respectively, at the same Au-ion fluence. The highest Au-ion fluence exhibited sudden vertical grain size drop to the sizes close to the pristine sample sizes.

Au distribution and damage profile by TOF-SIMS and TEM defect microstructure analysis

The TOF-SIMS profile of the in-depth concentration of Au seems to be in a reasonable agreement with the simulated profile as calculated by SRIM see Fig. 8a for W and Fig. 8b for W-Cr-Hf alloy. Slightly asymmetrical Au profile is observed by SIMS, where a small Au-implanted portion is identified in the depth creating non-normal depth distribution. Moreover, Au concentration–depth distributions were broader than in SRIM simulations; the depth distributions had right-hand tails differing in W and W-Cr-Hf samples. The broadened shapes of the implanted specie concentration–depth profiles have already been observed elsewhere as a consequence of distinct host structure modification and ion energy straggling during the ion bombardment [52–54] which can be connected to the distinct microstructure (distinct grain sizes, complex multielemental alloy versus single elemental material) of the irradiated materials [51]. This fact is supported by the distinct shapes of the Au-depth profiles in the W-Cr-Hf samples compared to the W samples. However, Au diffusion cannot be excluded in this case; as not all samples have the same broadening of the Au-depth profiles (see Fig. 8). In general, it is observed that the Au-ion calculated penetration depth is underestimated in comparison with the experimentally determined Au-concentration depth profiles due to an overestimation of the electronic stopping power for heavy incident ions in the SRIM program

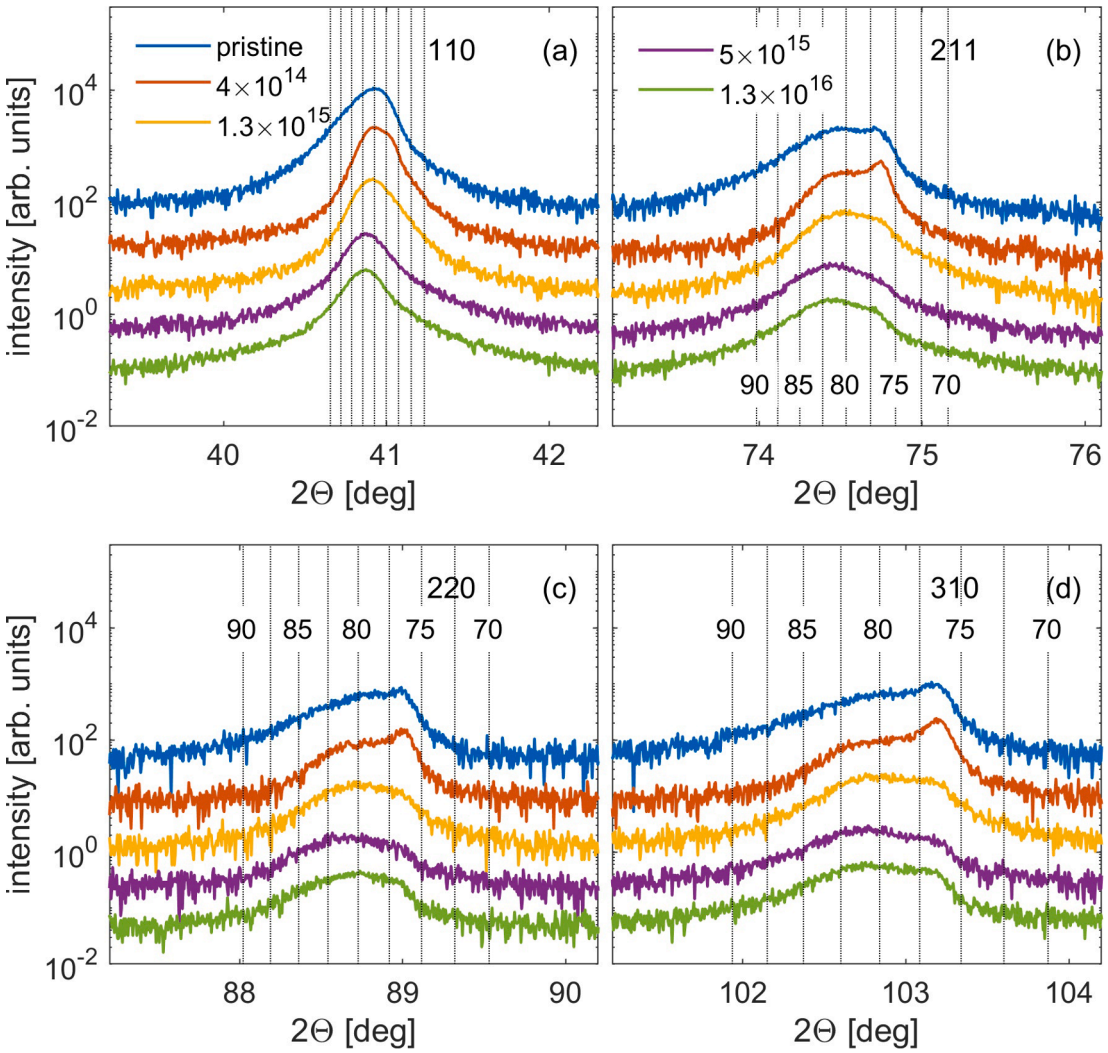

Fig. 7. XRD diffractograms of the W-Cr-Hf samples irradiated with Au-ions with the ion fluences 4×10^{14} cm^{-2}, 1.3×10^{15} cm^{-2} and 5×10^{15} cm^{-2} with the detail of (110), (211), (220) and (310) diffraction peaks in a), b), c), and d), respectively. Vertical lines indicate the W concentration scaling the vertical lattice parameter and consequently the diffraction peak position.

[54]; this effect can explain the Au maximum concentration being shifted into the depth versus SRIM calculation. SRIM calculation is based on input parameters – density, elemental composition and displacement energies for elements (see Table 1). The lower density of W-Cr-Hf material caused the higher calculated projected ranges of Au-ions compared to W material. In case of the W-Cr-Hf samples can play a role also the higher uncertainty of the used volume density in SRIM calculation.

We observed the asymmetry in the Au-ion distribution with the significant Au-distribution tail towards the depth in the W samples and in the W-Cr-Hf samples. This effect – distinct shape in comparison to Gaussian fit is presented in Fig. 8 and the mean values of the Gaussian fits are presented in Table 3. The maximum concentration is positioned in higher depth for the W-Cr samples for each Au-ion implantation fluence. The W samples exhibited the in-depth Au-concentration tail having similar slope for the fluences above 1.3×10^{15} cm^{-2}. We have chosen the concentrations c_{Au} in the depth range 800–1200 nm, as measured by SIMS, where the Au migration appears and where we identified non-Gaussian tail. For illustration, we plotted $\ln(c_{Au})$ versus *depth* for the Au-ion fluences 5×10^{15} cm^{-2} and 1.3×10^{15} cm^{-2} in the W and W-Cr-Hf samples (see Fig. 8c). We saw that after the linear fit the slope is slightly higher in the W samples. The concentration c_{Au} falls more progressively with the depth in the W samples. It seems that a portion of Au-implants migrates towards the sample depths and this portion is increased with the Au-ion fluence in W-Cr-Hf samples instead being very similar in the W samples above the implantation fluence 5×10^{15} cm^{-2}.

Figs. 9 and 10 show cross section STEM micrographs of the W-Cr-Hf and W samples. STEM identified the damaged surface layer in the pristine W-Cr-Hf sample, which was also evidenced in PAS analysis, however the thickness of the layer appeared in STEM has been broader about 300 nm (see Fig. 9a) in comparison to PAS (~90 nm). The damage profiles in dpa resulting from the implanted Au ions and from recoils were simulated with SRIM as a function of the penetration depth and are shown overlaid on top of the corresponding STEM micrograph (at 4×10^{14} cm^{-2}) for the W-Cr-Hf alloy (see Fig. 9b). The dpa depth profiles show the good agreement with the creation and appearance of the dense defect net according the dpa maximum in case of the lower Au-ion fluence see Fig. 9. However, we see as well the dislocations created in the depth beyond the predicted dpa depth profile. With the increase of the Au-ion fluence, higher density of longer dislocations appears in greater depths beyond the predicted Au-ion range exhibiting a kind of dislocation ordering in Fig. 9d, e.

In pure W alloy in Fig. 10, the STEM micrographs show different results compared to the W-Cr-Hf samples. The damage resulting from the implanted Au ions is less visible here, we can clearly recognize the grain

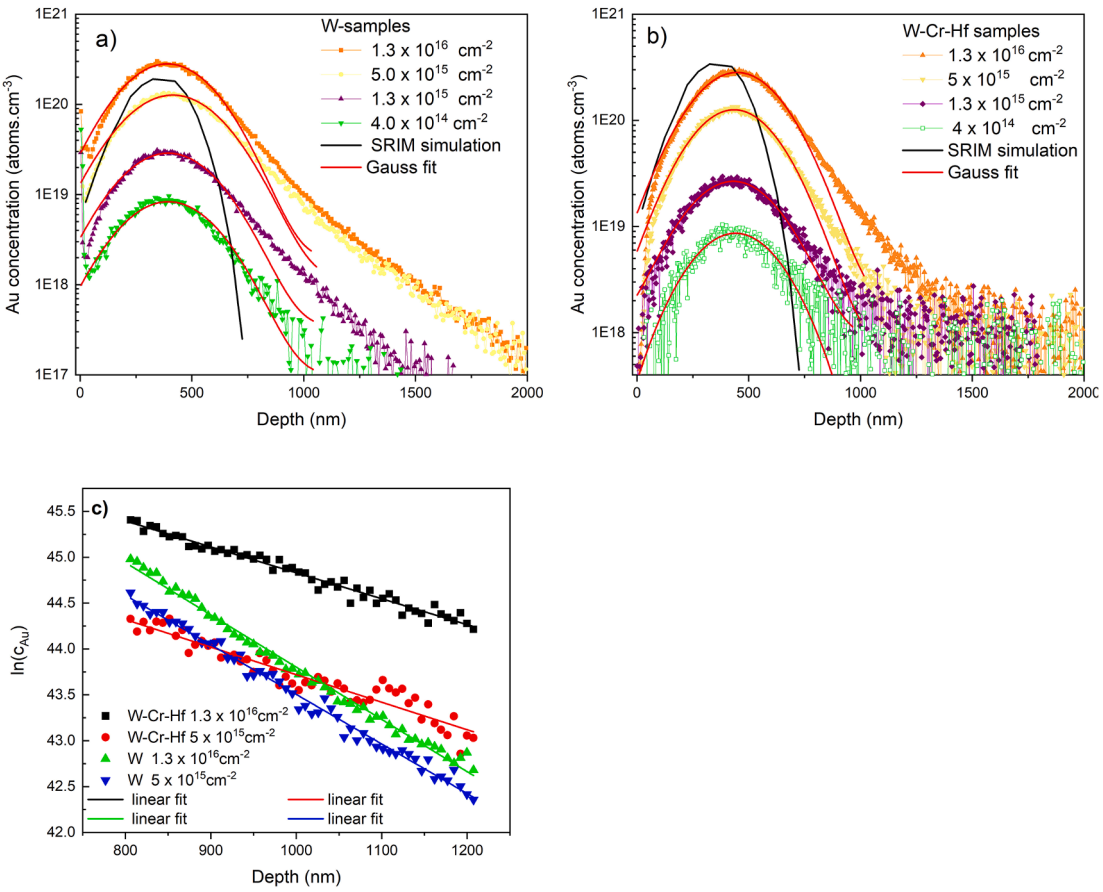

Fig. 8. Au concentration depth profiles obtained by TOF-SIMS for: a) W and b) W-Cr-Hf samples for various Au-ion irradiation fluences as compared to SRIM calculation. The Au-ion concentration c_{Au} is plotted as $\ln(c_{Au})$ versus depth in nm in the region 800–1200 nm using SIMS measured values in c). The linear fits of these plots are provided in c).

Table 3
The mean depth-values of the normal-distribution fit of the Au-concentration depth profiles determined from TOF-SIMS depth profiles in the W and W-Cr-Hf samples. The concentration maximum depth determined by SRIM calculation and as-extracted from TOF-SIMS analyses in the W-Cr-Hf and Wsample are compared.

Au-ion fluence [ions.cm^{-2}]	Mean depth of Au-concentration depth profile W samples [nm]	Mean depth of Au-concentration depth profile W-Cr-Hf samples [nm]
1.3×10^{16}	390	448
5×10^{15}	415	435
1.3×10^{15}	394	431
4×10^{14}	392	441
SRIM	321	349

boundaries (long bright lines). In the W samples irradiated with lowest ion fluence (4×10^{14} cm^{-2}), the dislocation net is practically invisible in the STEM micrographs (see Fig. 10a). The pristine sample image is not presented due to the similarity to the Fig. 10a. In case of the 1.3×10^{15} cm^{-2} ion fluence (see Fig. 10b), we observed defected layer thicker than predicted by SRIM. Due to the contrast in STEM micrographs we could assume mainly defect clusters evidenced in the depth appropriate to the projected range of Au-ions visible in the area around 300–400 nm below the surface. The defect clusters at the lower fluences increase in density and size according PAS analysis, finally the dislocations created in the depth beyond the simulated dpa profile start to be visible with the increase of the Au-ion fluence at 5×10^{15} cm^{-2} (see Fig. 10c and d), however, they do not reach the same density, length and depth below the surface as in the W-Cr-Hf alloy. Thus, the migration of defects is smaller in W alloy.

Thermal effusivity

In pure W, free electrons are the dominant heat carriers, while phonons contribute to merely around 10% [55,56,58]. The scattering mean free paths of these heat carriers are sensitive to crystalline imperfections (impurities, dislocations, vacancy clusters and grain boundaries etc.) [57,59].

In the Fig. 11, the thermal effusivity evolutions in time are plotted showing in fact the effusivity evolution through the depth. The thermal effusivity is a square root of thermal conductivity, specific heat and density and it expresses the ability of the material to extract the heat from surface to the material. The experimentally measured effusivity evolutions in time can be analysed and fitted to get thermal conductivity. The thin film thermal properties are varied in the model until the calculated effusivity temporal evolution fits the experimental one. The model is a three layer 1D model with surface absorption of laser light without thermal interface resistances between layers; the details are published in [60]. The measured thermal conductivity is the apparent thermal conductivity, because it also contains thermal interface resistance between the investigated thin film and substrate. The analytical model described in [39,60] was applied and the appropriate fits of the thermal effusivity curves are presented in Fig. 11, where the two or three layered system was taken into account for the fit. The last layer is the non-affected material.

The W sample implanted with the various Au-ion fluences exhibited effusivities from 11,500 to 16,400 Jm^{-2}. s$^{-1/2}$. K^{-1} compared to the pristine W sample with effusivity of 21000 ± 4500 Jm^{-2}. s$^{-1/2}$. K^{-1}. The

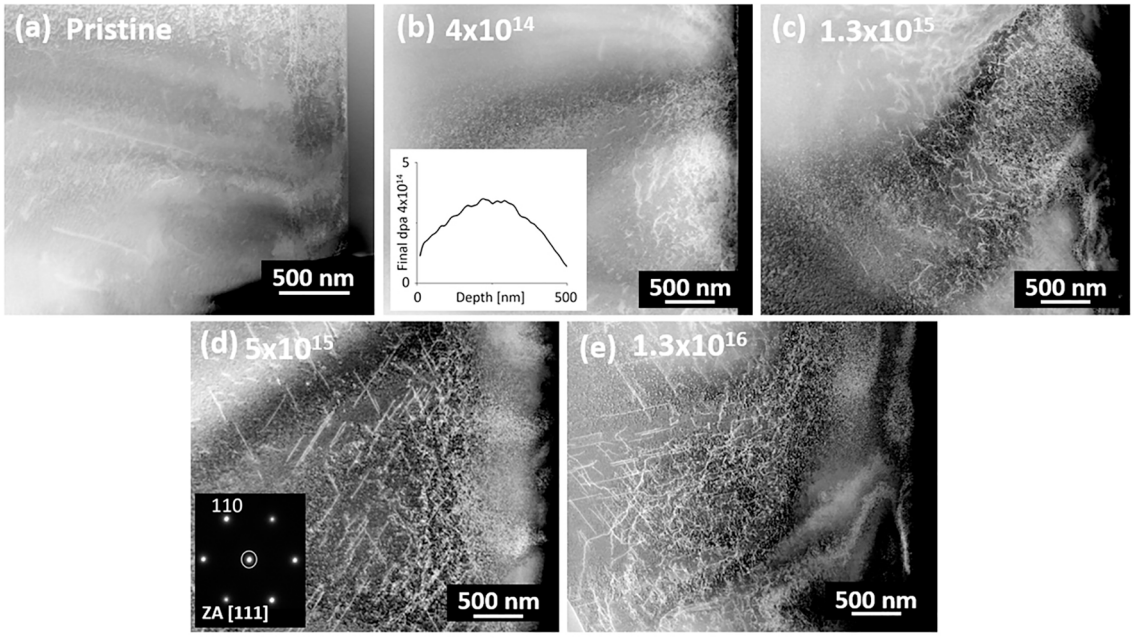

Fig. 9. Cross section STEM micrographs of W-Cr-Hf alloy for: (a) pristine sample, (b) sample irradiated with Au-ions with the ion fluences 4×10^{14} cm^{-2}, (c) 1.3×10^{15} cm^{-2}, (d) 5×10^{15} cm^{-2} and (e) with the ion fluence 1.3×10^{16} cm^{-2}. A simulated SRIM dpa depth profile for 5 MeV Au-ion irradiation with the fluences 4×10^{14} cm^{-2} is as an inset in (b). A [1 1 1] zone axis (ZA) diffraction pattern is as an inset in (d).

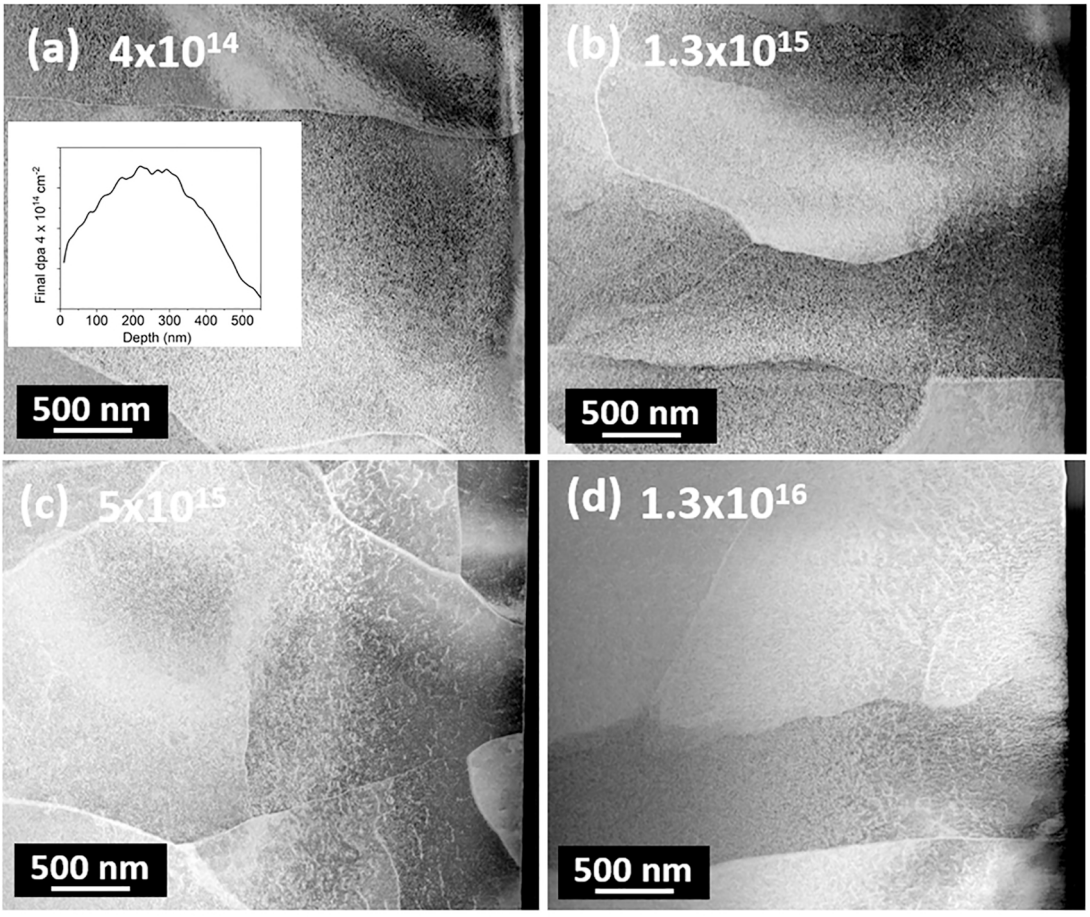

Fig. 10. Cross section STEM micrographs of W alloy for: (a) sample irradiated with Au-ions with the ion fluences 4×10^{14} cm^{-2}, (b) 1.3×10^{15} cm^{-2}, (c) 5×10^{15} cm^{-2} and (d) with the Au-ion fluences 1.3×10^{16} cm^{-2}.

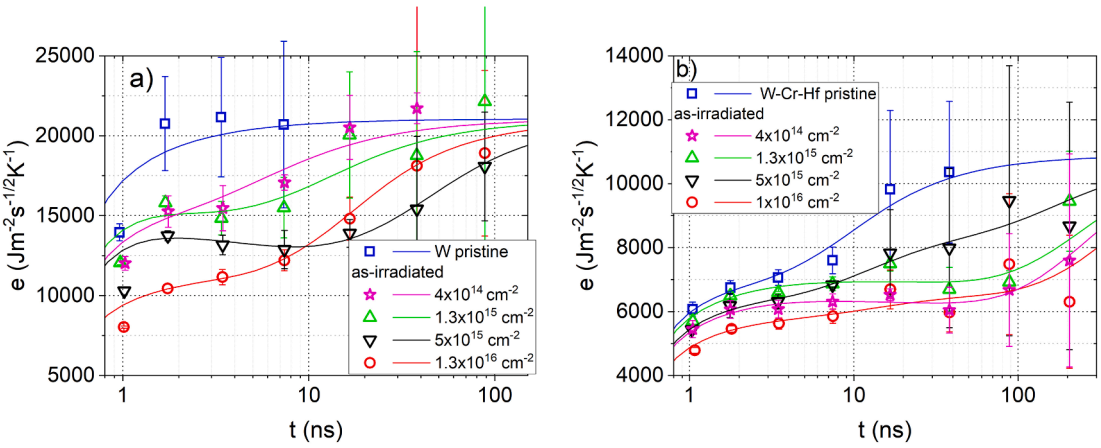

Fig. 11. The thermal effusivity of the pristine and the as-irradiated samples in W samples in a) and in W-Cr-Hf samples in b) as a function of time (roughly corresponding to depth). The fitted curves for the various layer thickness and thermal conductivities in the layers are depicted. The details of the fitted thermal effusivities in various depths are described in the text.

lowest thermal effusivity has been evidenced for the Au-ion highest fluence and the highest thermal effusivity for the lowest irradiation fluence (excluding the pristine sample) correlating well with the Au-ion fluence (see Fig. 10a and Table 4). It means that thermal properties and heat dissipation worsened gradually with the increasing Au-ion fluence and radiation damage. Simultaneously, at the highest Au-ion fluence the second layer exhibited the significant thermal properties decline in comparison to other fluences. The lowest thermal conductivity in W samples has been evaluated according to the model as 80, 60 and 52 W. m^{-1}. K^{-1} for the Au-ion fluences from 1.3×10^{15} to 1.3×10^{16} cm^{-2}, respectively, in the deeper layer 300–800 nm below the surface compared to the pristine value in this layer estimated as 174 W. m^{-1}. K^{-1}. The identified layer with the progressive decrease of the thermal conductivity is located around the Au-implanted maximal concentration depth (392–415 nm as it has been identified with SIMS exhibiting the Au redistribution into the depth up to 1 μm). In case of the highest fluence irradiated W-sample, the low thermal conductivity was observed from the surface up to 530 nm. These depths correspond well with the experimentally determined Au-concentration distribution as analysed by SIMS in Fig. 8 as well as with the SRIM calculated damage profiles presented in Fig. 1.

The W-Cr-Hf samples exhibited the depth profile of the thermal effusivity in the pristine sample already, moreover the thermal properties are worsened after the Au-ion irradiation without the clear correlation to the ion fluence and the worsening is not so progressive as in the case of the W samples. The depth profile of the thermal effussivity of W-Cr-Hf pristine sample differs from the pristine W-sample (see Fig. 11b). For W-Cr-Hf the effusivity exhibited depth evolution, where the thermal properties are enhanced towards the depth for the pristine as well as the Au-ion irradiated samples (see Table 4). Thermal effusivity fitting for the pristine W-Cr-Hf sample shows a 230 nm thick layer, where reduced thermal effusivity is observed. Such result is in accordance with the STEM findings. STEM identified the defected layer up to ~ 300 nm (see Fig. 9) in the pristine W-Cr-Hf sample.

In case of the W-Cr-Hf samples, the pristine surface layer has the effusivity of 7300 ± 400 Jm^{-2}. $s^{-1/2}$. K^{-1}. The thermal effusivity of implanted surfaces of W-Cr-Hf ranges from 6000 to 7100 Jm^{-2}. $s^{-1/2}$. K^{-1} in the first layer and from 6200 to 8800 Jm^{-2}. $s^{-1/2}$. K^{-1} in the second layer (compared to 11,000 Jm^{-2}. $s^{-1/2}$. K^{-1} for the pristine sample). The evaluated thermal conductivity of the surface layer about 250 nm thick is not significantly influenced by the Au-ion irradiation being from 12 to 17 W. m^{-1}. K^{-1} (compared to pristine sample value 18 W. m^{-1}. K^{-1}), contrary the deeper layer 250 – 1200 nm below the surface is sensitive on the irradiation and shows the decrease of the thermal conductivity from 40 W.m^{-1}. K^{-1} for pristine to value from 13 to 26 W. m^{-1}. K^{-1} for the irradiated samples without the correlation to the Au-ion fluence (see Table 4).

Discussion

We have observed a distinct damage accumulation in W and W-Cr-Hf alloy samples irradiated in a broad range of dpa with the 5 MeV Au-ions, where the latter samples exhibited lower damage accumulation and the sort of dynamic defect reorganization and possible annihilation with the increased ion fluence in the depth of the Au-ion projected range. Recently, radiation damage study in prospective materials for nuclear fusion was successfully imitated with heavy ions, where mainly Fe and Au of MeV energy-ions were employed to cause radiation damage [20]. In Ref. 51, ferritic/martensitic steel was irradiated by 6 MeV Au ions at room temperature (RT) and 400 °C to 25 dpa and 54 dpa. The lattice

Table 4
Thermal properties and thickness of the surface and subsurface layers of W and W-Cr-Hf samples after Au-ion irradiation as determined by the thermal effusivity measurement and model fitting.

Sample	Irradiation fluence (cm^{-2})	thermal effusivity ($Jm^{-2}.s^{-1/2}.K^{-1}$)		thermal conductivity ($Wm^{-1}K^{-1}$)		Thickness (nm)	
		first layer	second layer	first layer	second layer	first layer	second layer
W pristine	0	0	21,054		174		
W irradiated	4.0×10^{14}	0	16,355		105		500
W irradiated	1.3×10^{15}	17,485	14,276	120	80	300	300
W irradiated	5×10^{15}	15,961	12,363	100	60	280	650
W irradiated	1.3×10^{16}	0	11,510		52		530
W-Cr-Hf pristine	0	7310	10,897	18	40	230	
W-Cr-Hf irradiated	4.0×10^{14}	6561	6212	15	13	200	750
W-Cr-Hf irradiated	1.3×10^{15}	7104	6892	17	16	250	800
W-Cr-Hf irradiated	5×10^{15}	6673	8785	15	26	250	1000
W-Cr-Hf irradiated	1.3×10^{16}	5968	6673	12	15	250	1000

atomic displacement caused by irradiation produces interstitial atoms and vacancies, then dislocations and voids form through their movement and aggregation. [51].

In our experiment, the PAS analysis shows the damage accumulation with the increased Au-ion fluence in the deep implanted layer of the W samples, however PAS does not suggest variation in defect concentration, but rather an increase in defect size (we cannot exclude positron saturation trapping effects). We can conclude that damage accumulation in the W samples saturates in the depth (200–400 nm) for fluences above 1.3×10^{15} cm^{-2}, with the simultaneous release of defects from the subsurface layer which likely originate from the polishing procedure. The surface damage release after the irradiation could be connected to the effect observed in [66], where the kinetic energy from 5 MeV Si-ions irradiating W layers caused the activation of point defects which were removed from the crystal structure and in consequence led to the decrease of the compressive stress in the layer.

XRD did not observe significant modification of the diffraction pattern of the Au-irradiated W samples, however the evaluated density of dislocations is decreased slightly for the highest Au-ion fluence. However, the numerical values of the dislocation densities are unfavourably affected by the fact that the X-ray information depth is larger than the implantation depth so that the resulting densities have to be considered only qualitatively. The dislocation density decrease above the fluence 1.3×10^{15} cm^{-2} would not be evidenced by PAS due to saturation of the radiation damage in W matrix and less PAS sensitivity on such defects. We can also speculate that due to the saturation of positron trapping, PAS analysis did not identify dislocations, but defects like bi-vacancies, this being a general issue of positrons as a probe in the saturation regime. There were evidences in the literature [67], that dislocation line could act as a shallow positron trap and weak positron localization at dislocation can lead to diffusion along dislocation lines, thus this fact supports the previous suggestion as well. It should be emphasized that XRD gives information about the whole analysed volume, where various microstructural non-homogeneities are averaged. On the other hand, PAS analysis is sensitive on defect size, while XRD evidences the microstructural character and displaced atoms.

TEM analysis confirmed the maximum of defect in the predicted depth of the W samples according the Au-ion energy, where the higher density of larger defects is created in accordance with PAS. Dislocations are visible at the Au-ion fluence 5×10^{15} cm^{-2} being localized in the irradiated layer.

W-Cr-Hf alloys as prepared exhibited a different microstructure compared to the W samples. In our previous research, W-Cr-Hf exhibited grains about 5 μm in size, as analysed with Electron Backscattering Diffraction (EBSD), a scanning electron microscope (SEM) based technique that gives crystallographic information about the microstructure of a sample [24]. W samples microstructure has been investigated in [13] showing grains about 200 μm in length and tens of μm in lateral size. A role of grain boundary efficiency (different grain boundaries have different sink efficiencies) has been investigated in [61]. It was shown that fine-grained materials exhibit improved resistance to radiation damage due to the reduced grain size increasing the volume fraction of grain boundaries. The high density of grain-boundaries network serves as paths for diffusion/transport of defects. However, the sink efficiency was shown to depend on the overall grain boundary macroscopic character which includes both the misorientation angle and the grain boundary plane [62]. PAS in W-Cr-Hf showed smaller defect sizes induced by the Au-ion irradiation compared to the W samples; thus monovacancies and lower defect density saturating at lower fluences, showing evidence of its distinct radiation resistance and response under the Au-ion irradiation, but this phenomenon was evidenced in the buried layer, where the Au-ions were implanted. Simultaneously, the W-Cr-Hf samples exhibited defect density decrease in this depth at the Au-ion fluence above 5×10^{15}cm^{-2}. The size and defect concentration decrease is connected to the fact that preferably smaller defects (dislocations and monovacancies) are created in W-Cr-Hf in comparison to W samples. However, TEM analysis confirmed the maximal damage in the predicted depth and the smaller defect appearance in the dpa maximum depth at the highest Au-ion fluence. Surprisingly, defects seem to be very dynamic and gliding into large depth beyond the projected range of Au-ions and beyond the scope of PAS analysis. The appearance of less dense net of the larger dislocations in the deeper layer beyond the Au-ion projected range is observed with the increasing Au-ion fluence. XRD identified slight modification of vertical grain sizes with increasing irradiation fluence. Energetic ions seem to dynamically change the vertical grain sizes and transfer energy to point defects, release the pre-existing strain. This fact would be beneficial feature of the solid solution of the W-Cr-Hf [24], dynamically responding to the radiation damage, creating smaller defects in the upper layer with simultaneous migration of defects into the depth. This phenomenon could be somewhat connected to the fact, that the lowest activation energy of diffusion is referred for W in Cr (386 ± 33 kJ. mol^{-1}) investigating various combination of W and Cr. Localized Cr-rich regions at grain boundaries can be created during the sintering which act as a diffusion paths for W displaced atoms [24].

SIMS analysis of the Au-depth profiles evidenced asymmetry of the Au-concentration depth profiles versus normal distribution in both types of samples. The Au-concentration depth profiles showed the concentration maximum being in a higher discrepancy with the theoretical SRIM calculation, but it can be connected to the fact, that W-Cr-Hf density is not so precisely known as in case of W samples. On the other hand, the lower slope of the Au-concentration in the depth beyond the maximum in the W-Cr-Hf samples could be connected to more pronounced Au-migration into the depth. It would be connected to the observed migration of defects and their accumulation in the form of large dislocations in the layers beyond the irradiated depth in STEM. In more complex, multi-elemental solid solution alloys, the annihilation of defect might be connected to the obstacles [67] as e.g. grain boundaries as sink and annihilation centers, lower-sized defect clusters are created with the increased ion fluence in the W-Cr-Hf samples in the implanted layer where Au is located. Simultaneously, one should take into account the different internal morphology, grain sizes and the radiation resistance of both investigated materials. The W-Cr-Hf exhibited fine and smaller grains [24] and smaller defect size and density (the PAS results in this experiment) and the Au-migration into the depth is more pronounced.

Analysis of thermal properties shows a progressive decrease of the thermal effusivity with irradiation in the depth appropriate to the Au-ion penetration; the subsurface layer, exhibiting the worsening of thermal properties, increases in thickness with the Au-ion fluence in accordance with SIMS results. The thermal properties in the W-Cr-Hf samples seem to be similarly influenced by the Au-ion irradiation, although for the pristine samples the surface already exhibited thermal effusivity depth profile, where the surface layer has the lower thermal effusivity, probably connected with the originally defected surface layer (proved by PAS and TEM) caused by the polishing procedure. PAS confirmed the thicker defected layer in pristine W-Cr-Hf samples compared to W samples which is recovered after the Au-ion irradiation and thermal effusivity is not modified in the shallow sub-surface layers.

We can conclude that W-Cr-Hf structure responded distinctly to the Au-ion irradiation: smaller size defects were created in the implanted layer . PAS identified significant decrease of the defect size; there are several scenarios possible: defects can be lost at grain boundaries or can be absorbed by other defect clusters [64]. However, from TEM it seems that smaller defect clusters are created in the buried layer according the Au-ion range, but dislocation net of oriented dislocations is created in very deep layers.

On the other hand, in W samples the Au-ion irradiation induced defects which were retained in the material and they can create obstacles for gliding dislocations [63]. Thermal transport properties can be degraded by grain boundaries along the direction of heat transfer which can significantly increase scattering of electrons [61]. The origin of

thermal property degradation must be tied with the nature, size and population of radiation defects in materials, this fact is exhibited in the thermal effusivity depth profiles in the W-Cr-Hf samples showing the worse surface layer quality in the pristine sample already.

Our TEM and PAS results showed interesting dislocation behaviour, which has been observed also in Fe-Cr steel [65]. In Vogel et al. [65], two dislocation loop layers in steel irradiated with 5 MeV Au-ions were evidenced, first one close to the surface with larger dislocation loops appropriately to the predicted dpa maximum and the second deeper layer with the injected interstitials with much smaller dislocation loops. In our case in W-Cr-Hf alloy, the band structure is observed as well, but we see opposite trend concerning the sizes of the dislocations which creates very dense net of small dislocations close to the dpa maximum, where the size and density cannot be determined clearly and larger separated dislocation in the depth. Preferential orientation of the large dislocations observed in W-Cr-Hf above the ion fluence 5×10^{15}cm^{-2} could be connected to the findings in Ref. 65, where the fraction of 111-type loops was 75% in case of an irradiated bulk steel sample. We cannot clearly identify dislocation loops orientations in our experiment due to the deformations however this would be further task in future.

Conclusion

We have been followed specific defect dynamics in W-Cr-Hf alloys compared to W samples in the broad range of dpa from 1 up to 98 dpa. Broad spectrum of analytical methods (PAS, XRD, SIMS and TEM) offered novel information about the distinct defect accumulation, defect character and mobility in the irradiated layers and beyond in both materials. Thermal properties were followed as a function of the Au-ion fluence. Au-ion irradiation of W-Cr-Hf alloy samples demonstrated a surprising trend of defect size and concentration decrease in the sub-surface buried layer containing the implanted Au-ions. A thin defected sub-surface layer in the pristine samples was released after the Au-ion irradiation in both materials as a consequence of ion-energy transfer. We can conclude that W-Cr-Hf structure responded distinctly to the Au-ion irradiation: smaller size defects were created in the implanted layer and higher Au-ion dissipation in the depth compared to W samples has been observed. The radiation damage was found to be saturated at average value of 3 dpa for pure W. W-Cr-Hf alloy exhibits a higher defect migration into the deeper layer without clear damage saturation in the irradiated depth.

CRediT authorship contribution statement

A. Macková: Conceptualization, Investigation, Visualization. **S. Fernandes:** Investigation, Data curation, Funding acquisition. **J. Matejíček:** Methodology, Resources. **M. Vilémová:** Methodology, Resources. **V. Holý:** Investigation, Data curation. **M.O. Liedke:** Investigation, Visualization, Data curation. **J. Martan:** Investigation, Visualization, Data curation. **M. Vronka:** Investigation, Data curation. **M. Potoček:** Investigation, Data curation. **P. Bábor:** Investigation, Data curation. **M. Butterling:** Investigation, Data curation. **A.G. Attallah:** Methodology, Data curation. **E. Hirschmann:** Methodology, Data curation. **A. Wagner:** Methodology, Data curation. **V. Havránek:** Supervision.

Declaration of Competing Interest

The authors declare that they have no known competing financial interests or personal relationships that could have appeared to influence the work reported in this paper.

Acknowledgements

The research has been carried out at the CANAM (Centre of Accelerators and Nuclear Analytical Methods) infrastructure LM 2015056. This publication has been supported by the project Strategy AV 21 of the Czech Academy of Sciences. Part of the experimental work was also supported by CzechNanoLab project LM2018110 at CEITEC Nano Research Infrastructure and at LNSM Research Infrastructure funded by MEYS CR. The research was also supported by the Ministry of Education, Youth and Sports of the Czech Republic (LABIR-PAV project, No. CZ.02.1.01/0.0/0.0/18_069/0010018).

References

[1] R. Rayaprolu, S. Möller, R. Abernethy, M. Rasinski, J.C. Haley, C.h. Linsmeier, Indentation testing on 3 MeV proton irradiated tungsten, Nucl. Mater. Energy 25 (2020) 100776, https://doi.org/10.1016/j.nme.2020.100776.
[2] M. Abdou, N.B. Morley, S. Smolentsev, A. Ying, S. Malang, A. Rowcliffe, M. Ulrickson, Blanket/first wall challenges and required r&d on the pathway to demo, Fusion Eng. Des. 100 (2015) 2–43, https://doi.org/10.1016/j.fusengdes.2015.07.021.
[3] C.-H. Huang, M.R. Gilbert, J. Marian, Simulating irradiation hardening in tungsten under fast neutron irradiation including re production by transmutation, J. Nucl. Mater. 499 (2018) 204–215, https://doi.org/10.1016/j.jnucmat.2017.11.026.
[4] H. Bolt, V. Barabash, W. Krauss, J. Linke, R. Neu, S. Suzuki, N. Yoshida, ASDEX Upgrade Team. Materials for the plasma-facing components of fusion reactors, J. Nucl. Mater. 329–333 (2004) 66–73, https://doi.org/10.1016/j.jnucmat.2004.04.005.
[5] M. Rieth, R. Doerner, A. Hasegawa, Y. Ueda, M. Wirtz, Behavior of tungsten under irradiation and plasma interaction, J. Nucl. Mater. 519 (2019) 334–368, https://doi.org/10.1016/j.jnucmat.2019.03.035.
[6] J. Knaster, A. Moeslang, T. Muroga, Materials research for fusion, Nat. Phys. (2016) 424–434, https://doi.org/10.1038/nphys3735.
[7] R.G. Abernethy, Predicting the performance of tungsten in a fusion environment: a literature review, Mater. Sci. Technol. 33 (4) (2016) 388–399, https://doi.org/10.1080/02670836.2016.1185260.
[8] R.W. Harrison, On the use of ion beams to emulate the neutron irradiation behaviour of tungsten, Vacuum 160 (2019) 355–370, https://doi.org/10.1016/j.vacuum.2018.11.050.
[9] R. Neu, J. Riesch, J.W. Coenen, J. Brinkmann, A. Calvo, S. Elgeti, C. García-Rosales, H. Greuner, T. Hoeschen, G. Holzner, F. Klein, F. Koch, C. Linsmeier, A. Litnovsky, T. Wegener, S. Wurster, J.H. You, Advanced tungsten materials for plasma-facing components of DEMO and fusion power plants, Fusion Eng. Des. 109–111 (2016) 1046–1052, https://doi.org/10.1016/j.fusengdes.2016.01.027.
[10] A. Litnovsky, T. Wegener, F. Klein, C.h. Linsmeier, M. Rasinski, A. Kreter, B. Unterberg, J.W. Coenen, H. Du, J. Mayer, C. Garcia-Rosales, A. Calvo, N. Ordas, Smart tungsten alloys as a material for the first wall of a future fusion power plant, Nucl. Fusion 57 (6) (2017), https://doi.org/10.1088/1741-4326/aa6816.
[11] A. Calvo, C. García-Rosales, F. Koch, N. Ordás, I. Iturriza, H. Greuner, G. Pintsuk, C. Sarbu, Manufacturing and testing of self-passivating tungsten alloys of different composition, Nucl. Mater. Energy 9 (2016) 422–429, https://doi.org/10.1016/j.nme.2016.06.002.
[12] C. Yin, D. Terentyev, S. Van Dyck, A. Stankovskiy, R.H. Petrov, T. Pardoen, Effect of high-temperature neutron irradiation on fracture toughness of ITER-specification tungsten, Phys. Scr. 2020 (2020) T171, https://doi.org/10.1088/1402-4896/ab54d7.
[13] J. Matějíček, J. Veverka, C.h. Yin, M. Vilémová, D. Terentyev, M. Wirtz, M. Gago, A. Dubinko, H. Hadraba, Spark plasma sintered tungsten – mechanical properties, irradiation effects and thermal shock performance, J. Nucl. Mater. 542 (2020) 152518.
[14] G.S. Was, S.J. Zinkle, Toward the Use of Ion Irradiation to Predict Reactor Irradiation Effects, Reference Module in Materials Science and Materials Engineering, In book, 2020.
[15] N.W. Phillips, H. Yu, S. Das, D. Yang, K. Mizohata, W. Liu, R. Xu, R.J. Harder, F. Hofmann, Nanoscale lattice strains in self-ion implanted tungsten, Acta Mater. 195 (2020) 219–228, https://doi.org/10.1016/j.actamat.2020.05.033.
[16] D.R. Mason, X. Yi, M.A. Kirk, S.L. Dudarev, Elastic trapping of dislocation loops in cascades in ion-irradiated tungsten foils, J. Phys. Cond. Matter 26 (2014) 375701, https://doi.org/10.1088/0953-8984/26/37/375701.
[17] A.E. Sand, K. Nordlund, S.L. Dudarev, Radiation damage production in massive cascades initiated by fusion neutrons in tungsten, J. Nucl. Mater. 455 (1–3) (2014) 207–211, https://doi.org/10.1016/j.jnucmat.2014.06.007.
[18] A. Khan, R. Elliman, C. Corr, J.J.H. Lim, A. Forrest, P. Mummery, L.M. Evans, Effect of rhenium irradiations on the mechanical properties of tungsten for nuclear fusion applications, J. Nucl. Mater. 477 (2016) 42–49, https://doi.org/10.1016/j.jnucmat.2016.05.003.
[19] D.E.J. Armstrong, P.D. Edmondson, S.G. Roberts, Effects of sequential tungsten and Helium ion implantation on nano-indentation hardness of tungsten, Appl. Phys. Lett. 102 (2013) 251901, https://doi.org/10.1063/1.4811825.
[20] Z. Zhang, E. Hasenhuetl, K. Yabuuchi, A. Kimura, Evaluation of Helium effect on ion-irradiation hardening in pure tungsten by nano-indentation method, Nucl. Mater. Energy 9 (2016) 539–546, https://doi.org/10.1016/j.nme.2016.06.010.
[21] C.L. Dube, P.K. Kulriya, D. Dutta, P.K. Pujari, Y. Patil, M. Mehta, P. Patel, S. S. Khirwadkar, Positron annihilation lifetime measurement and X-ray analysis on 120 MeV Au+7 irradiated polycrystalline tungsten, J. Nucl. Mater. 467 (2015) 406–412, https://doi.org/10.1016/j.jnucmat.2015.05.029.

[22] C.h. Linsmeier, M. Rieth, J. Aktaa, T. Chikada, A. Hoffmann, J. Hoffmann, A. Houben, H. Kurishita, X. Jin, M. Li, A. Litnovsky, S. Matsuo, A. von Müller, V. Nikolic, T. Palacios, R. Pippan, D. Qu, J. Reiser, J. Riesch, T. Shikama, R. Stieglitz, T. Weber, S. Wurster, J.-H. You, Z. Zhou, Development of advanced high heat flux and plasma-facing materials, Nucl. Fusion 57 (9) (2017) 092007, https://doi.org/10.1088/1741-4326/aa6f71.

[23] O. El-Atwani, E. Esquivel, M. Efe, E. Aydogan, Y.Q. Wang, E. Martinez, S.A. Maloy, Loop and void damage, during heavy ion irradiation on nanocrystalline and coarse grained tungsten: Microstructure, effect of dpa rate, temperature, and grain size, Acta Mater. 149 (2018) 206–219, https://doi.org/10.1016/j.actamat.2018.02.035.

[24] M. Vilémová, K. Illková, F. Lukáč, J. Matějíček, J. Klečka, J. Leitner, Microstructure and phase stability of W-Cr alloy prepared by spark plasma sintering, Fusion Eng. Des. 127 (2018) 173–178, https://doi.org/10.1016/j.fusengdes.2018.01.012.

[25] J.F. Ziegler et al., SRIM: The stopping and range of ions in matter, Version SRIM-2013. http://www.srim.org/.

[26] ASTM E521, 96(2009) Standard practice for neutron irradiation damage simulation by charged particle irradiation.

[27] P. Jung, Production of atomic defects in metals by irradiation. in Atomic Defects in Metals (ed. Ullmaier, H.) 25, 6–7 (Springer-Verlag, 1991).

[28] A.Yu. Konobeyev, U. Fischer, Yu.A. Korovin, S.P. Simakov, Evaluation of effective threshold displacement energies and other data required for the calculation of advanced atomic displacement cross-sections, Nucl. Energy Technol. 3 (3) (2017) 169–175, https://doi.org/10.1016/j.nucet.2017.08.007.

[29] R. Krause-Rehberg, H.S. Leipner, Positron annihilation in semiconductors, Defect Stud. (1999).

[30] Filip Tuomisto, Ilja Makkonen, Defect identification in semiconductors with positron annihilation: Experiment and theory, Rev. Mod. Phys. 85 (4) (2013) 1583–1631, https://doi.org/10.1103/RevModPhys.85.1583.

[31] M.O. Liedke, W. Anwand, R. Bali, S. Cornelius, M. Butterling, T.T. Trinh, A. Wagner, S. Salamon, D. Walecki, A. Smekhova, H. Wende, K. Potzger, Open volume defects and magnetic phase transition in Fe 60 Al 40 transition metal aluminide, J. Appl. Phys. 117 (2015) 163908, https://doi.org/10.1063/1.4919014.

[32] W. Anwand, G. Brauer, M. Butterling, H.R. Kissener, A. Wagner, Design and Construction of a Slow Positron Beam for Solid and Surface Investigations, Defect Diffus. Forum 331 (2012) 25–40, https://doi.org/10.4028/www.scientific.net/DDF.331.25.

[33] A. Wagner, W. Anwand, A.G. Attallah, G. Dornberg, M. Elsayed, D. Enke, A.E. M. Hussein, R. Krause-Rehberg, M.O. Liedke, K. Potzger, T.T. Trinh, Positron annihilation lifetime spectroscopy at a superconducting electron accelerator, J. Phys. Conf. Ser. 791 (2017) 012004, https://doi.org/10.1088/1742-6596/791/1/012004.

[34] A. Wagner, M. Butterling, M.O. Liedke, K. Potzger, R. Krause-Rehberg, Positron annihilation lifetime and Doppler broadening spectroscopy at the ELBE facility, AIP Conf. Proc. (2018) 040003, https://doi.org/10.1063/1.5040215.

[35] J.V. Olsen, P. Kirkegaard, N.J. Pedersen, M. Eldrup, PALSfit: A new program for the evaluation of positron lifetime spectra, Phys. Status Solidi. 4 (2007) 4004–4006, https://doi.org/10.1002/pssc.200675868.

[36] E.H. Khan, M.H. Weber, M.D. McCluskey, Formation of Isolated Zn Vacancies in ZnO Single Crystals by Absorption of Ultraviolet Radiation: A Combined Study Using Positron Annihilation, Photoluminescence, and Mass Spectroscopy Phys, Rev. Lett. 111 (2013) 017401, https://doi.org/10.1103/PhysRevLett.111.017401.

[37] F.A. Stevie, L. Sedlacek, P. Babor, J. Jiruse, E. Principe, K. Klosova, FIB-SIMS Quantification using TOF-SIMS with Ar and Xe plasma sources, Surf. Interface Anal. 46 (2014) 285–287, https://doi.org/10.1002/sia.5483.

[38] J. Martan, O. Herve, V. Lang, Two-detector measurement system of pulse photothermal radiometry for the investigation of the thermal properties of thin films, J. Appl. Phys. 102 (2007) 064903, https://doi.org/10.1063/1.2778642.

[39] J. Martan, Optical layer development for thin films thermal conductivity measurement by pulsed photothermal radiometry, Rev. Sci. Instrum. 86 (2015) 014902, https://doi.org/10.1063/1.4904876.

[40] A. van Veen, H. Schut, M. Clement, J.M.M. de Nijs, A. Kruseman, M.R. IJpma, VEPFIT applied to depth profiling problems, Appl. Surf. Sci. 85 (1995) 216–224, https://doi.org/10.1016/0169-4332(94)00334-3.

[41] L.C. Smedskjaer, M. Manninen, M.J. Fluss, An alternative interpretation of positron annihilation in dislocations, J. Phys. F Met. Phys. 10 (10) (1980) 2237–2249, https://doi.org/10.1088/0305-4608/10/10/019.

[42] J. Čížek, O. Melikhova, Z. Barnovská, I. Procházka, R.K. Islamgaliev, Vacancy clusters in ultra fine rained metals prepared by severe plastic deformation, J. Phys. Conf. Ser. 443 (2013) 012008, https://doi.org/10.1088/1742-6596/443/1/012008.

[43] M.J. Puska, R.M. Nieminen, Theory of positrons in solids and on solid surfaces, Rev. Mod. Phys. 66 (3) (1994) 841–897, https://doi.org/10.1103/RevModPhys.66.841.

[44] X. Hu, T. Koyanagi, M. Fukuda, Y. Katoh, L.L. Snead, B.D. Wirth, Defect evolution in single crystalline tungsten following low temperature and low dose neutron irradiation, J. Nucl. Mater. 470 (2016) 278–289, https://doi.org/10.1016/j.jnucmat.2015.12.040.

[45] L.Yu. Dubov, S.V. Stepanov, D. Terentyev, Yu.V. Funtikov, Yu.V. Shtotsky, V. S. Stolbunov, V. Efimov, K. Gutorov, Annealing of radiation-induced defects in tungsten: Positron annihilation spectroscopy study, J. Nucl. Mater. 517 (2019) 148–151.

[46] B. Girault, P. Villain, E. Bourhis, P. Goudeau, P.O. Renault, X-ray diffraction analysis of the structure and residual stresses of W/Cu multilayers, Surf. Coat. Technol. 201 (7) (2006) 4372–4376. ff10.1016/j.surfcoat.2006.08.034.

[47] J.B. Chen, C.N.J. Wagner, J. Appl. Phys. 33 (1963) 2073–2077.

[48] M. Wilkens, The determination of density and distribution of dislocations in deformed single crystals from broadened X-ray diffraction profiles, Phys. Status Solidi. A 2 (1970) 359–370, https://doi.org/10.1002/pssa.19700020224.

[49] T. Ungár, J. Gubicza, G. Ribárik, A. Borbély, Crystallite size distribution and dislocation structure determined by diffraction profile analysis: principles and practical application to cubic and hexagonal crystals, J. Appl. Cryst. 34 (2001) 298–310, https://doi.org/10.1107/S0021889801003715.

[50] A. Van Veen, H.A. Filius, J. De Vries, K.R. Bijkerk, G.J. Rozing, D. Segers, Hydrogen exchange with voids in tungsten observed with TDS and PA, J. Nucl. Mater. 155–157 (1988) 1113–1117, https://doi.org/10.1016/0022-3115(88)90478-3.

[51] Shi-Ke Zhang, Wei Ning, Zhien Wang, Hu, Liao, Jiali Yang, Yuanyou Liu, Ning Yang Jijun, Microstructural evolution and hardening effect of 12Cr2W2Mn ferritic/martensitic steel under Au-ions irradiation, J. Alloy. Compd. 835 (2020), 155360, https://doi.org/10.1016/j.jallcom.2020.155360.

[52] N.M. Lyadov, A.I. Gumarov, V.F. Valeev, V.I. Nuzhdin, R.I. Khaibullin, I. A. Faizrakhmanov, Optical and electrical studies of ZnO thin films heavily implanted with silver ions, J. Phys. Conf. Ser. 572 (2014) 012022, https://doi.org/10.1088/1742-6596/572/1/012022.

[53] A. Macková, P. Malinsky, A. Jágerová, Z. Sofer, D. Sedmidubský, K. Klímová, R. Böttger, S. Akhmadaliev, Damage accumulation and structural modification in a- and c-plane GaN implanted with 400-keV and 5-MeV Au + ions, Surf. Interface Anal. 50 (11) (2018) 1099–1105, https://doi.org/10.1002/sia.6403.

[54] S. Moll, Y. Zhang, Z. Zhu, P.D. Edmondson, F. Namavar, W.J. Weber, Comparison between simulated and experimental Au-ion profiles implanted in nanocrystalline ceria, Nucl. Instr. Meth. B 15 (2013) 93–97, https://doi.org/10.1016/j.nimb.2012.12.119.

[55] L. Hu, B.D. Wirth, D. Maroudas, Thermal conductivity of tungsten: effects of plasma-related structural defects from molecular-dynamics simulations, APL 111 (2017) 081902, https://doi.org/10.1063/1.4986956.

[56] L.L. Snead, S.J. Zinkle, D.P. White, Thermal conductivity degradation of ceramic materials due to low temperature, low dose neutron irradiation, J. Nucl. Mater. 340 (2005) 187–202, https://doi.org/10.1016/j.jnucmat.2004.11.009.

[57] D. Choi, The electron scattering at grain boundaries in tungsten films, Microelectron. Eng. 122 (5) (2014) 5–8, https://doi.org/10.1016/j.mee.2014.03.012.

[58] Y. Xiaoou, Lei Zhang, Wentuo Han, Jiao Chen, Pingping Liu, Yanwei Lv, Jiupeng Song, Luwei Xue, Diancheng Geng, Kenta Yoshida, Takeshi Toyama, Qian Zhan, Farong Wan, Somei Ohnuki, Yasuyoshi Nagai, Defect characterization, mechanical and thermal property evaluation in CVD-W after low-dose neutron irradiation, Int. J. Refract Metal Hard Mater. 85 (2019) 105004, https://doi.org/10.1016/j.ijrmhm.2019.105004.

[59] Xiao-Yu Ding, Jia-Qin Liu, Lai-Ma Luo, Xu. Qiu, Xiang Gao, Jian-Jun Huang, Yu. Bin, Jian-Gang Li, Wu. Yu-Cheng, TEM studies of 1 MeV Fe+ ion-irradiated W alloys by wet chemical method: high-temperature annealing and deuterium retention, Nucl. Fusion 59 (2019) 016008, https://doi.org/10.1088/1741-4326/aaeaee.

[60] D.L. Balageas, J.C. Krapez, P. Cielo, Pulsed photothermal modeling of layered materials, J. Appl. Phys. 59 (1986) 348, https://doi.org/10.1063/1.336690.

[61] P. Zarnas, R. Dingreville, B. Muntifering, K. Hattar, B.L. Boyce, J. Qu, Statistical analysis of the interaction between irradiation-induced defects and triple junctions, Adv. Model. Simul. Eng. Sci. (2020) 7:5, https://doi.org/10.1186/s40323-020-0140-0.

[62] M. Barr, G.A. Vetterick, K.A. Unocic, K. Hattar, X.-M. Bai, M.L. Taheri, Anisotropic radiation-induced segregation in 316L austenitic stainless steel with grain boundary character, Acta Mater. 67 (2014) 145–155, https://doi.org/10.1016/j.actamat.2013.11.060.

[63] S. Das, Recent advances in characterising irradiation damage in tungsten for fusion power, SN Appl. Sci. 1 (2019) 1614, https://doi.org/10.1007/s42452-019-1591-0.

[64] L. Ciupiński, O.V. Ogorodnikova, T. Płociński, M. Andrzejczuk, M. Rasiński, M. Mayer, K.J. Kurzydłowski, TEM observations of radiation damage in tungsten irradiated by 20 MeV W ions, Nucl. Instr. Meth. B 317 (2013) 159–164, https://doi.org/10.1016/j. nimb.2013.03.022.

[65] K. Vogel, P. Chekhonin, C. Kaden, M. Hernández-Mayoral, S. Akhmadaliev, F. Bergner, Depth distribution of irradiation-induced dislocation loops in an Fe-9Cr model alloy irradiated with Fe ions: The effect of ion energy, Nucl. Mater. Energy 27 (2021) 101007, https://doi.org/10.1016/j.nme.2021.101007.

[66] K. Hlushko, A. Mackova, J. Zalesak, M. Burghammer, A. Davydok, C. Krywka, R. Daniel, J. Keckes, J. Todt, Ion irradiation-induced localized stress relaxation in W thin film revealed by cross-sectional X-ray nanodiffraction, Thin Solid Films 722 (2021) 138571, https://doi.org/10.1016/j.tsf.2021.138571.

[67] Lu. Chenyang, Ke Jin, Laurent K. Béland, Feifei Zhang, Taini Yang, Liang Qiao, Yanwen Zhang, Hongbin Bei, Hans M. Christen, Roger E. Stoller, Lumin Wang, Direct Observation of Defect Range and Evolution in Ion-Irradiated Single Crystalline Ni and Ni Binary Alloys, Sci. Rep. 6 (2016) 19994, https://doi.org/10.1038/srep19994.